energy&fuels

Editors' Choice

pubs.acs.org/EF

Article

Influence of Ordered Mesoporous Oxides in Plasma-Assisted Ammonia Synthesis

Published as part of Energy & Fuels special issue "Celebrating Women in Energy Research".

Sonia E. Arumuganainar, Stavroula Sartzetakis, Cole W. Hullfish, Bruce E. Koel, and Michele L. Sarazen*

Cite This: *Energy Fuels* 2024, 38, 23150−23166

Read Online

ACCESS | Metrics & More | Article Recommendations | Supporting Information

ABSTRACT: Widespread implementation of dielectric barrier discharge (DBD)-assisted NH_3 synthesis, a nascent technology operating under sustainable, ambient conditions, is hindered by low energy yields due to, in part, poor fundamental understanding. Porous oxides used to support metal nanoparticle catalysts have shown significant energy yield contributions for DBD-assisted NH_3 synthesis even without metal. Using an AC-powered, coaxial, single-stage reactor at 16 kV with equimolar (N_2/H_2) feed, we measured NH_3 synthesis rates in the presence of different nonordered oxides, ordered SiO_2 structures (SBA-15 and MCM-41), and ordered Al-incorporated analogues (γ-Al_2O_3-coated with varying Al-loadings and Al-substitution, respectively: Al_2O_3-SBA-15 and Al-MCM-41). We systematically quantified NH_3 energy yield dependence on pore structures and material identities (i.e., ordered pores and Al incorporation) known to facilitate higher DBD-assisted NH_3 synthesis rates. SBA-15 displayed a higher steady-state energy yield than MCM-41, indicating that framework type is a crucial factor, with both ordered porous systems outperforming fumed SiO_2. 10 wt % Al maximized in situ NH_3 uptake among the various Al loadings, exhibiting a higher steady-state energy yield and similar power to SBA-15. However, Al-MCM-41 had a similar steady-state energy yield and lower power than MCM-41, likely due to the extended γ-Al_2O_3 surface that has a dielectric constant higher than that of SiO_2. Both Al-incorporated analogues benefit from surface acid sites that can adsorb NH_3 in situ, resulting in higher overall NH_3 energy yields than that of their parent ordered SiO_2. Al_2O_3-SBA-15 shielded more NH_3 than Al-MCM-41, likely due to a higher acid site density than the acid site identity. Thus, Al incorporation via γ-Al_2O_3 coating more successfully improves the NH_3 energy yield; together with the high-performing ordered framework, these analogues are potential metal catalyst supports with promising energy yields for DBD-assisted synthesis of NH_3 and other chemicals.

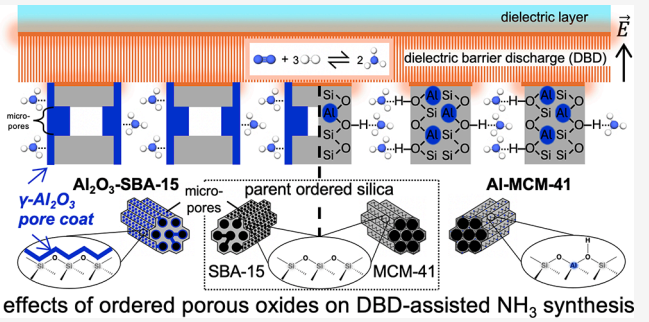

INTRODUCTION

Many essential industrial chemicals require high energy demand (e.g., high temperatures to activate stable bonds and frequently high pressures) even in the presence of catalysts. This is exacerbated by the large scale of these processes and their slow start up/shut down, requiring centralized, stable energy sources like fossil fuels instead of dispersed, renewable energy sources, leading to significant CO_2 emissions. Haber-Bosch ammonia (NH_3) production, for example, requires temperatures of 573−773 K to activate nitrogen (N_2) and high pressures ($1.5–2.0 \times 10^4$ kPa),[1] emitting 450 Mt of CO_2 in 2020—the largest chemical sector contributor and currently responsible for 1% of the global energy demand.[2] Given that NH_3 demand is projected to increase with the increasing global population (and resultant fertilizer demand),[3] as well as its use as a molecular energy carrier,[4−8] reducing the carbon footprint for its production is crucial to curtail emissions globally.

Considering the decades of optimization for Haber-Bosch,[9] more tractable gains in sustainability for NH_3 synthesis will likely come from alternative energy sources, like nonthermal plasmas (NTPs).[10−12] While NTPs are also explored for processes associated with NH_3 synthesis, such as catalyst pretreatment to create N and O vacancies or as an upstream process to photocatalysis or electrocatalysis, we focus on direct NH_3 production from NTPs.[13] In direct NH_3 production, the NTP utilizes high-energy electrons to collide with reactants while operating at (near) ambient conditions; these collisions result in the generation of vibrationally and electronically excited molecules and radicals that are able to react at mild conditions.[1,14,15] However, NTPs do not differentiate in

Received: July 5, 2024
Revised: October 21, 2024
Accepted: October 21, 2024
Published: November 15, 2024

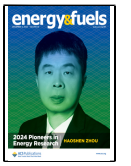

https://doi.org/10.1021/acs.energyfuels.4c03270
Energy Fuels 2024, 38, 23150−23166

dissociating the N_2 reactant versus NH_3 product, leading to decomposition of NH_3 formed in the NTP, lowering NH_3 yields and energy efficiencies.[16−19] Hybrid NTP-catalyst systems combine catalyst selectivity with the low-temperature advantage of NTPs,[13] such that the generated excited species can react in the bulk gas phase or on the catalyst surface.[1] AC-powered, dielectric barrier discharges (DBDs) in single-stage, coaxial packed bed reactors are a common rector configuration, where catalysts facilitate dissociation of excited (usually N_2)[20] species.[21−27] However, the energy yields (amount of product collected per unit energy supplied)[28] of these reactors are still trailing current industrial processes.[21−23]

The development of strategies to improve the DBD-assisted energy yield for NH_3 as well as other reactions is hindered, in part, by its poorly understood mechanism. With a single-stage catalyst bed, surface-catalyzed and bulk DBD-phase NH_3 production occur concurrently and are difficult to decouple[26] because the synergetic interactions between the DBD and the dielectric porous solids are not additive (i.e., process descriptors, such as reaction rates, of the DBD-catalytic process exceed that of the thermal catalytic and homogeneous DBD processes combined).[26,28] Furthermore, since the excited species in the DBD are short-lived, the evolving interactions between the DBD and catalyst lead to varying physiochemical properties and reaction pathways in a single-stage reactor.[13] Previous work has reported improved N_2-to-NH_3 conversions in the presence of γ-Al_2O_3 packing[25] and increased N_2 vibrational temperatures from higher electron energies in the presence of TiO_2 packing,[29] both relative to the absence of a packed bed. Similarly, comparable NH_3 production rates and energy yields were measured on γ-Al_2O_3 with and without Ru nanoparticles.[30] Even in a different reaction system (DBD-assisted dry reforming of CH_4), the reactant conversion generally decreased with metal loading.[31] These dielectric materials can affect DBD-induced charging via storage of electrical energy, influencing surface reactions and even the nature of the DBD, which is comprised of filamentous microdischarges when at ambient pressures.[32] However, it has been shown that catalyst beds can lead to more spatially confined microdischarges and surface discharges that enhance the DBD.[28,29,33−36] In fact, it has been suggested that the packed materials affect NH_3 production more significantly via its modifications to the DBD than direct surface catalysis.[37] Further, packed materials in a single-stage reactor likely interact with NTPs in general and modify them (by varying the discharge gap at a minimum). These materials are typically dielectric in nature (e.g., porous oxides) such that these plasma−support interactions have an effect specific to DBD plasmas compared to other NTPs. Selecting catalysts based on their interaction with the DBD is key to increasing the energy yield of the NH_3 synthesis reaction.[13]

That being said, the exact interplay between the solid and the DBD is not understood; as such, we aim to deduce systematically how common properties of catalyst design, i.e., material identity and porous structure (pore diameter, order, and internal surface area), can affect reactor performance, namely, NH_3 energy yield. In terms of porous oxide identity, γ-Al_2O_3 has shown a higher NH_3 yield than SiO_2, likely due to its higher dielectric constant.[38] The porous structure complicates how the packed bed interfaces with the DBD microdischarges. Upon contact with a nonporous surface, the DBD simply forms a uniform sheath;[39] for large enough pores (the threshold diameter is known as the Debye length), the sheath can penetrate pores and envelope the pore walls, though this effect can vary across reactor configurations. Most studies agree that the microporous and mesoporous scales of the typical support are smaller than the Debye length, especially for atmospheric DBDs,[40−42] so the internal pore volume and surface area would not contribute to the DBD-support synergy. However, porous beads have exhibited synergistic enhancement of the N_2-to-NH_3 conversion compared to nonporous beads of similar dielectric constants.[43] The discrepancy was attributed to the textured external surface (controlled by the pore size and order) creating additional surface microdischarges.[44] It was also postulated that the internal surface exhibited catalytic activity due to excited, reactive species diffusing from the external bulk DBD.[43] This is consistent with another example of mesoporous γ-Al_2O_3 and SiO_2 gels containing hydrocarbons immobilized within the pores that underwent DBD-assisted oxidization, which could only be facilitated by the diffusion of excited oxidative species into the pore volume to react with the hydrocarbons.[45] In fact, small SiO_2 pore structures inaccessible to the DBD have shown higher dry reforming CH_4 conversions than large pore structures that allow DBD penetration because the huge loss in surface area with large pores negates the benefits of DBD penetration, whereas the diffusion of excited species into small pores can utilize a much larger area for surface reactions.[46] Moreover, ordered porosity was demonstrated to enhance NH_3 energy yield compared to nonordered analogues with the same elemental composition (e.g., ordered SBA-15 versus fumed SiO_2).[47] The observed enhancement was attributed (at least partially) to the utilization of the high internal surface area of ordered materials by diffused excited species; a recent study comparing ordered SiO_2 frameworks measured a higher NH_3 energy yield on SBA-15 than the similar MCM-41 framework, which the authors attributed to the easier transport of excited species within the mesopore channels of SBA-15 via interconnecting micropores.[48] As such, the effect of the material and porosity of the support on NH_3 production rates, DBD properties, and ultimately energy yields is key for their optimization via catalyst design. Here, to minimize impacts of varied pore sizes, we probed the porosity effects on the NH_3 energy yield with ordered mesoporous materials, which offer narrow pore size distributions (PSDs) and synthetic control over pore sizes and surface areas of porous oxide supports.

The diffusion of (excited) species from the bulk DBD into mesoporous oxides, without plasma penetration, avails another support design strategy to improve the NH_3 energy yield: adsorbing product NH_3 within the pores via appropriate functionalization of the pore walls (i.e., acid sites). NH_3 synthesis is equilibrium-limited, so adsorption of NH_3 within the support shields it from bulk DBD-assisted decomposition, shifting the equilibrium in the forward direction.[21,22,26] This has been demonstrated with zeolites, where in situ recovery of NH_3 shielded within zeolite 4A (via temperature-swing desorption post-DBD-assisted reaction) doubled the energy yield to 2.3 g NH_3/kWh.[49] Similarly, γ-Al_2O_3 offers acid site functionality and has been utilized in many DBD-assisted NH_3 synthesis studies over SiO_2-based supports.[23,25,30,50−52]

The ordered materials explored for DBD-assisted NH_3 synthesis (i.e., SBA-15 and MCM-41) have demonstrated utilization of their internal surface area for shielding NH_3 and shifting the reaction equilibrium in favor of NH_3 synthesis;[48,53] however, since they are SiO_2-based, they can only take up NH_3 through weak physisorption. A similar structure with surface

https://doi.org/10.1021/acs.energyfuels.4c03270
Energy Fuels 2024, 38, 23150−23166

acid site functionality would allow for NH_3 recovery via desorption post-reaction to improve the NH_3 energy yield. Synthetic control over γ-Al_2O_3 ordered structures is hindered by less established, more involved templating syntheses.[54−58] Furthermore, ordered γ-Al_2O_3 has lower surface areas (200−500 m^2/g) compared to SBA-15 (700−1000 m^2/g),[59,60] so if the SBA-15 pore walls were functionalized with a similar density of acid sites, it would have a greater NH_3 adsorption capacity that likely translates to more NH_3 uptake that is shielded from decomposition during the DBD-assisted reaction.[48,49] Thus, we coated SBA-15 with γ-Al_2O_3 according to published procedures,[59−61] introducing (primarily Lewis) acid sites to the high surface area of SBA-15 for NH_3 adsorption and achieving an ordered mesoporous γ-Al_2O_3 surface with known relationships between the synthetic aging conditions and the pore size and surface area.[62−64] Al-incorporated MCM-41 (Al-MCM-41) provided a different surface functionalization (i.e., acid site identity and density as well as surface dielectric properties) on a similar framework, introducing isolated Bronsted acid sites without an γ-Al_2O_3 coat or its dielectric characteristics.

These Al-incorporated and parent ordered SiO_2 were tested in our AC-powered, coaxial, single-stage DBD reactor at a fixed applied voltage to understand how the different surface functionalization via Al incorporation in packed beds affects the NH_3 outflow rates and power supplied over time, which in turn determine the overall NH_3 energy yields. The ordered materials were tested alongside nonordered porous oxides to understand the effect of introducing ordered porosity, especially for the Al-incorporated samples that have not been studied before in this application. We also tested commonly used nonordered commercial beads, which result in a more open packing, to benchmark the effect of the different particle packing structures on microdischarges and DBD-assisted reactor performance. Despite the ubiquity of larger (sub)-millimeter-scale particles (with more open packing), smaller (sub)micron particles with tighter packing have exhibited higher conversions for DBD-assisted dry reforming of CH_4.[31] On the other hand, smaller particles have exhibited larger breakdown voltages resulting in partial discharges for DBD-assisted CO_2 reduction, which lowered the overall reactor performance despite the higher conversions.[65] The packed bed effects are clearly highly nuanced and thus sensitive to reactor configurations and reaction systems, such that we aim to study these effects within our DBD-assisted reactor for NH_3 synthesis. The quantification of the energy yield enhancement arising from introducing ordered pores and incorporating Al will better inform how these known beneficial properties of porous oxide supports can be harnessed in the catalyst design to improve the energy yield of the DBD-assisted synthesis of NH_3 and other commodity chemicals.

EXPERIMENTAL SECTION

Materials. Nonordered, porous oxides were purchased from commercial vendors: γ-Al_2O_3 powder (Alfa Aesar, 99.997% metals basis), fumed SiO_2 powder (H-5, CAB-O-SIL), γ-Al_2O_3 beads (Saint-Gobain NorPro, 0.9 mm dia.), SiO_2 beads (SaintGobain NorPro, 1.5 mm dia.), and nonporous SiO_2 beads (Benchmark Scientific, 1.0 mm dia.). Ordered porous oxides were either purchased, MCM-41-based materials (MCM-41 (Sigma-Aldrich, CAS Number: 7631-86-9, 5 g) and Al-MCM-41 (Sigma-Aldrich, CAS Number: 1318-02-1, 5 g)), or synthesized in-house, SBA-15-based materials (SBA-15 and Al_2O_3-SBA-15), using Pluronic-123 (P-123, Sigma-Aldrich, $M_n \sim 5800$), concentrated HCl (Ward's Science, 37%), tetraethyl orthosilicate (TEOS, Tokyo Chemical Industry, >97.0%), and aluminum nitrate nonahydrate ($Al(NO_3)_3{\cdot}9H_2O$, Chem-Impex International Incorporated, 99.88%, ACS reagent). Potassium bromide (KBr, Acros Organics, 99+ %, ACS reagent) was used as the powder diluent for Fourier transform infrared (FTIR) analysis. All of the starting materials were used as received without further purification.

Synthesis of SBA-15 and Al_2O_3-SBA-15. The SBA-15-based materials were synthesized in-house based on literature procedures.[59,60] 12 g of P-123 (12 g) was dissolved in 375 mL of 1.9 M HCl solution (prepared from concentrated HCl) at room temperature for 3 h, after which 25.2 g of TEOS was added. The mixture was stirred at 313 K for 20 h and then left undisturbed to age at 373 K for 24 h. The final product was obtained after vacuum-dried filtration and calcination under static air at 823 K for 6 h. Al_2O_3-SBA-15 of varying composition (i.e., 5, 7.5, 10, 12.5, and 15 wt % Al; differentiated using x-Al_2O_3-SBA-15 where the prefix x represents the target Al weight loading) was synthesized via wetness impregnation of SBA-15 following a reported procedure,[59] in which as-synthesized SBA-15 was mixed for 24 h in an aqueous solution of $Al(NO_3)_3$ with a corresponding concentration to the target Al loading. The mass of the $Al(NO_3)_3{\cdot}9H_2O$ precursor added to 12 mL of DI water to form this solution is calculated using the following equation.

$$m_{Al(NO_3)_3\cdot 9H_2O} = \frac{x \times m_{SBA\text{-}15}}{M_{Al} - x_{Al_2O_3} \times \frac{1}{2} \times M_{Al_2O_3}} \times M_{Al(NO_3)_3\cdot 9H_2O}$$

$m_{SBA\text{-}15}$ and $m_{Al(NO_3)_3\cdot 9H_2O}$ are the masses of SBA-15 and $Al(NO_3)_3{\cdot}9H_2O$ used in the composite synthesis, respectively, while M_{Al}, $M_{Al_2O_3}$, and $M_{Al(NO_3)_3\cdot 9H_2O}$ are the molar masses of Al, Al_2O_3, and $Al(NO_3)_3{\cdot}9H_2O$, respectively. After wetness impregnation, the aqueous solvent was evaporated overnight at 353 K; then, the recovered powder was dried at 373 K for 4 h and finally calcined under static air at 823 K for 5 h to obtain x-Al_2O_3-SBA-15.

Material Characterization. FTIR spectra were collected for SBA-15 and Al_2O_3-SBA-15 samples on a Nicolet iS50 infrared spectrophotometer to determine the completeness of the γ-Al_2O_3 coverage of the siliceous surface in the composites. Each sample (2 wt %) was mixed with KBr and pressed into pellets at 10,000 psi for 3 s utilizing a hydraulic press (Carver model 4350 L) and 13 mm die set. The data density was reduced to every 20th data point for ease of plotting. Porosity was measured via N_2 physisorption performed with a Micromeritics 3Flex physisorption unit (SBA-15 and 10-Al_2O_3-SBA-15 were evaluated both pre- and post-pelletization). All samples were degassed at 383 K under a mild vacuum (125 Torr) for at least 24 h prior to N_2 physisorption. The collected N_2 adsorption and desorption isotherms (77 K) were used to obtain the Brunauer−Emmett−Teller (BET) internal surface area and the Barrett−Joyner−Halenda (BJH) adsorption PSD of the porous oxides. The density functional theory (DFT) micropore volumes of the porous oxides were determined as the cumulative DFT pore volume up to 2 nm from the cumulative DFT pore volume distribution as a function of the pore width. This plot was obtained using a N_2 Tarazona—nonlocal DFT model with Esf = 30.0 K, assuming a cylindrical geometry and utilizing data across the full relative pressure range. A Micromeritics Autochem II 2920 unit was used to perform NH_3-temperature-programmed desorption (TPD) measurements to evaluate the ex situ NH_3 uptake capacity of the various porous oxides. Equilibrium NH_3 uptake was established over 1 h at 373 K (to approximate the reactor temperature with DBD-induced heating), after which the temperature was ramped at 10 K min^{-1}, and NH_3 outflow was recorded as a function of the temperature during the desorption. The temporal profile of NH_3 outflow was integrated to back calculate the equilibrium NH_3 uptake.

Images of Al_2O_3-SBA-15 and commercial beads were procured using a Quanta environmental scanning electron microscope with a Schottky field emission gun, and an Evex energy dispersive X-ray (EDX) spectroscopy accessory was used to approximate elemental composition via elemental mapping. Transmission electron microscopy (TEM) images of Al_2O_3-SBA-15 were obtained with a Talos

https://doi.org/10.1021/acs.energyfuels.4c03270
Energy Fuels 2024, 38, 23150−23166

F200X scanning/TEM (S/TEM) with a Thermofisher Super X EDX accessory equipped with 4 EDX detectors located above the sample position. Details of microscopy sample preparation can be found in the Supporting Information.

Catalyst Preparation. The nonordered powders, alongside the powder-structured ordered materials, were pelletized at 1000 psi for 3 s utilizing a hydraulic press (Carver model 4350 L) and 13 mm die set, then crushed and sieved to obtain larger particles between 1 and 2 mm. Surface hydroxylation (via incipient wetness impregnation) of fumed SiO_2 facilitates easier pelletization since hydrogen bonding between particles improves agglomeration. As such, incipient wetness impregnation of 3 g fumed SiO_2 was achieved with 8.5 mL of deionized water over 2 h, then left to dry at room temperature for 22 h undisturbed. The recovered powder was then calcined under static air at 723 K (achieved with a ramp rate of 2 K min^{-1}) and held for 3 h prior to pelletization.

DBD-Assisted NH_3 Synthesis Reactions (with Pre- and Post-treatment Procedure). A simplified schematic of the reactor configuration and coaxial cross section is provided in Figure S1. The coaxial DBD reactor consisted of two concentric quartz tubes, an outer tube (10.5 mm I.D., 12.75 mm O.D., 15 in. length) and an inner tube (4 mm I.D., 6.35 mm O.D., 13 in. length), with the porous oxide packing filling the annular gap to form a 2 in. bed. The inner tube was sheathed with a stainless-steel rod, which served as an electrode and was thus connected to an AC power source (Information Unlimited, PVM500-2500) at 20 kHz. The outer tube was wrapped with copper mesh over the packed bed, which served as the other electrode and was connected back to the power source with a 1000 pF capacitor in series. The potential drop across the capacitor and the reactor was measured by Tektronix voltage probes (TPP0201 with a 200 MHz bandwidth and P6015A with a 75 MHz bandwidth, respectively) and recorded on an oscilloscope (Instek, GDS-1054B), providing a Lissajous plot of charge (product of capacitance (1000 pF) and the potential drop across the capacitor) versus the potential drop across the reactor. The power supplied to the DBD can then be calculated from multiplying the area enclosed by the Lissajous plot obtained without any data smoothing or linear fitting with the AC frequency (20 kHz).

The reactor was operated at 760 Torr and a peak-to-peak applied voltage of 16 ± 0.2 kV, in a room temperature environment without any external heating/cooling to control the internal temperature, with equimolar N_2 and H_2 feed set to 40 sccm each. The actual flow rate for each gas was demonstrated to be within 5% of the set-point with a flow meter. The applied voltage was manually monitored in real-time via the oscilloscope and adjusted to a constant value, as opposed to maintaining a constant power supply to the DBD-assisted reactor, in order to provide a similar driving force for high-energy electron generation in the DBD. DBD-assisted NH_3 synthesis in the presence of a catalyst is also known to be strongly dependent on applied voltage (hypothesized to be due to the highly ionized reaction gas and enhanced surface reactions).[13] The energy yields used to ultimately evaluate the relative performance of the various ordered and nonordered porous oxides are also normalized by the power supplied to the DBD. The DBD was generated for 8000 s over the packed bed, with the applied voltage and Lissajous plot collected every 300 s. Abrupt changes in the applied voltage were corrected back to 16 kV by adjusting the dial setting on the power source (i.e., adjusting the power supplied to the DBD); once stabilized, the applied voltage and Lissajous plots were recorded every 300 s for another hour and once more at 7800 s. The power supplied to the DBD-assisted reactor was evaluated at each time point the Lissajous plot was captured; all the recorded Lissajous plots thus provide a temporal profile of the power supplied throughout the DBD-assisted reaction.

Prior to DBD exposure, the quartz tube was enclosed in a furnace (MTI Corporation, OTF-1200X-S) such that the reactor volume (and any porous oxide packed within) was dried in situ under a 40 sccm N_2 flow at 773 K (a ramp rate of 10 K min^{-1} with 1 h dwell). Once the oven program was concluded, the reactor was allowed to cool to room temperature (monitored by using the furnace thermocouple) under the same N_2 inert flow. After the reactor reached room temperature, a 40 sccm H_2 flow was introduced alongside the existing N_2 flow for the DBD-assisted reaction, following the procedure described above. After the DBD exposure, adsorbed NH_3 within the porous oxide packing (if any) was recovered in situ under 40 sccm N_2 inert flow via TPD, where the reactor was heated to 973 K with a ramp rate of 10 K min^{-1} and held for 1 h. Throughout all three stages, the composition of the reactor effluent, which was continuously fed to a 10 cm-long quartz cell equipped with two CaF_2 windows (HT gas cell, Pike Technologies), was quantified with an online-sampling Bruker INVENIO R FTIR deuterated lanthanum alanine-doped triglycine sulfate detector. Each spectrum was an average of 100 scans collected with a resolution of 2 cm^{-1} over 148 s, representing the effluent composition at the midpoint of this duration to obtain a continuous temporal profile, with a 10 s wait between each spectrum. The reactor effluent was transported to the Pike cell through a 1/8 in. stainless steel Swagelok tube; NH_3 retention on the tube wall was minimized via heating to 383−403 K via heating tape coiled around the tube that was connected to a Variac transformer. The temperature of the tube wall was monitored during DBD generation (at the same time points, Lissajous plots were recorded), as well as at the start and end of the pre- and post-treatment. NH_3 concentration was quantified with the area of the peak at 3300−3325 cm^{-1}, integrated within the OPUS software associated with the Bruker FTIR, and translated to a NH_3 mole fraction via calibration curves. The product of the NH_3 mole fraction with the reactant flow rate (80 sccm) yields the NH_3 volumetric outflow rate, which is converted to a molar basis by using the ideal gas law. Here, we use the NH_3 outflow rate because it does not deconvolute contributions from the rate of the reverse NH_3 decomposition reaction as well as the NH_3 in situ adsorption rate.

For pulsing experiments, after steady-state NH_3 outflow was established during a typical reaction run with predrying treatment (as outlined above), the DBD was shut off until the NH_3 outflow recorded dropped to zero for two consecutive measurements (which took about 10 min). The DBD was then re-established using the same power setting recorded at steady-state NH_3 outflow prior to the shut-off. The system was left undisturbed until steady-state NH_3 outflow was re-established, with three consecutive measurements reporting the same NH_3 outflow, after which the DBD was shut off again. This duration of DBD exposure was defined as one "pulse", and the process was repeated for at least two more pulses with constant DBD shut-off periods in between pulses (following the time taken to reach NH_3-free outflow before the first pulse, ∼10 min).

NH_3 Energy Yield Calculations. The steady-state energy yield is obtained from the ratio of the mean steady-state NH_3 outflow during the DBD-assisted reaction (average of the last 10 data points in its temporal profile) and the steady-state power supplied at 7900 s (from the final recorded Lissajous plot). The overall energy yield is the combined NH_3 collected (i.e., during the DBD-assisted reaction and during the TPD post-reaction) normalized by the energy supplied to the DBD-assisted reactor during the reaction. The former is obtained by integrating the NH_3 outflow temporal profiles corresponding to the DBD-assisted reaction and TPD post-reaction, while the latter is obtained from integrating the temporal profile of the power supplied to the DBD-assisted reactor. The energy supplied for heating the reactor during in situ TPD is not accounted for, as previous work has shown that it is less significant than the power supplied to the reactor,[49] and in situ NH_3-TPD can potentially be integrated with waste heat or also electrified.

RESULTS AND DISCUSSION

Material Characterization of SBA-15-Based Materials with Varying γ-Al_2O_3 Coating. The synthesis procedure for Al_2O_3-SBA-15 of varying x wt % Al loading (x-Al_2O_3-SBA-15) was evaluated with material and textural characterization before use in DBD-assisted NH_3 production. FTIR spectra (Figure 1) of all the SBA-15-based materials exhibited the bulk Si−O−Si stretch at 1086 cm^{-1},[59,66] which was used to scale and align all the spectra (full spectra can be found in the

https://doi.org/10.1021/acs.energyfuels.4c03270
Energy Fuels 2024, 38, 23150−23166

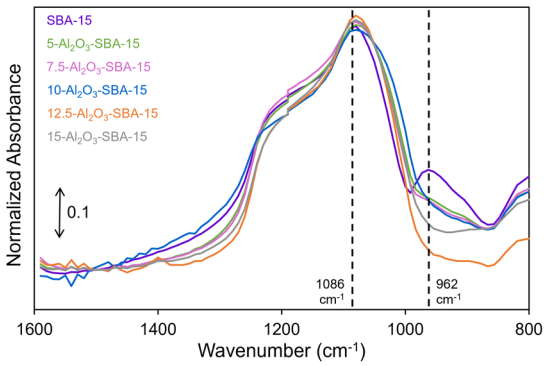

Figure 1. Truncated FTIR absorbance spectra of the SBA-15-based materials, showing the absorbance bands corresponding to Si−O−Si stretch at 1086 cm^{-1} and Si−OH bend at 962 cm^{-1}.

Supporting Information; Figure S2). Only the uncoated SBA-15 exhibited a band at 962 cm^{-1} corresponding to a surface Si−OH bend;[59,66] the absence of this band in the spectra of the Al_2O_3-SBA-15 composites suggests that the incorporated γ-Al_2O_3 leaves no exposed siliceous surface of SBA-15 across all Al loadings of the composite, providing full γ-Al_2O_3 surface functionality.

N_2 physisorption measurements at 77 K (Figure 2a) of the SBA-15-based materials yielded Type IV(a) adsorption−desorption isotherms as defined by IUPAC, characterized by a hysteresis loop at intermediate relative pressures and a steep curve at low relative pressures that indicate mesoporous and microporous structures, respectively.[67] Although the isotherms for uncoated SBA-15 and the Al_2O_3-SBA-15 composites fall under the same general category, there were clear deviations in isotherm shape (i.e., more horizontal hysteresis loop and less steep isotherm at low relative pressures for Al_2O_3-SBA-15). The shifts in the isotherms are indicative of differences in the porous structure, which we attribute to the incorporation of γ-Al_2O_3 into the SBA-15 framework, corroborated by the decrease in BET surface area (extracted from the N_2 adsorption−desorption isotherms) with increasing Al loading (Table 1). The Type H1 hysteresis loop (parallel, nearly vertical adsorption−desorption isotherms) in the uncoated SBA-15 isotherm indicates uniform mesopores, which are supported by its sharp, narrow BJH adsorption PSD (Figure 2b). The Al_2O_3-SBA-15 composites showed a reduction in height and width of their PSD relative to uncoated SBA-15, where full widths at half maximum (fwhm) (obtained from Gaussian peak fitting detailed in the Supporting Information; Figure 2c) were similar (within error) for the Al_2O_3-SBA-15 composites across the various Al weight loadings. Their fwhm is only slightly larger than that of uncoated SBA-15, indicating that γ-Al_2O_3 incorporation into SBA-15 preserves the pore order despite the progressively more horizontal hysteresis loop in the isotherms. Type H1 hysteresis loops typically plateau at high relative pressures due to limiting adsorption, but the slight hysteresis loop observed at high relative pressures for all SBA-15-based materials (Figure 2a) resembled a Type H3 loop instead, which indicates some disorder in the form of particle agglomeration.[67,68]

Table 1. DFT Micropore Volume, BET Surface Area, and BJH Adsorption Mean Pore Diameters of the SBA-15-Based Materials

Al loading (%)	DFT micropore volume (cm^3/g)	BET surface area (m^2/g)	BJH adsorption mean pore diameter (nm)
0	0.22	860	7.8
5	0.096	510	7.4
7.5	0.083	450	7.2
10	0.064	410	7.0
12.5	0.034	280	6.8
15	0.026	250	6.9

The decreasing gradient of the isotherms at low relative pressures with increasing Al loading suggests fewer accessible micropores, which is supported by the decreasing DFT micropore volume extracted from the N_2 adsorption−desorption isotherms (Table 1). Micropores are found along the mesopore channel walls in SBA-15,[69,70] so the decreasing DFT micropore volume indicates that the additional γ-Al_2O_3 is penetrating and coating the mesopore channels of SBA-15, blocking access to the micropores on the channel walls. This is corroborated by the decreasing mean pore size of BJH adsorption PSD with increasing Al loading and, together with the consistent fwhm of the PSD, indicates that an even coating of γ-Al_2O_3 is achieved along the SBA-15 pore walls.

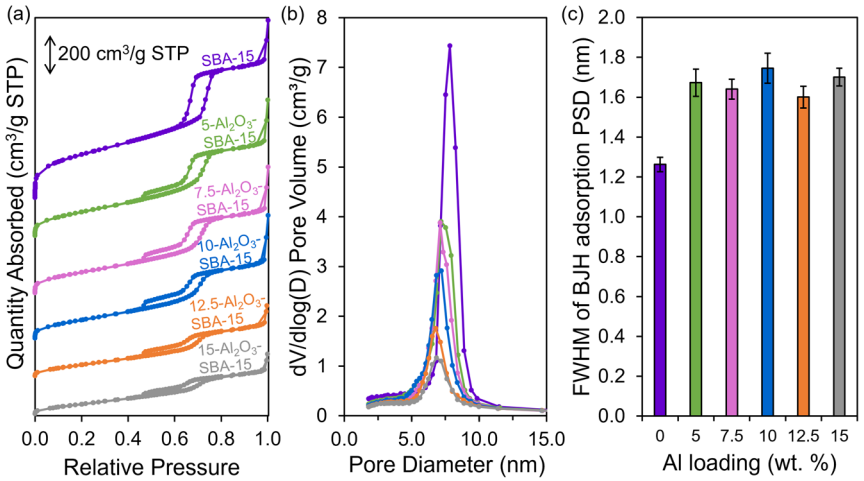

Figure 2. (a) N_2 adsorption−desorption isotherms at 77 K, (b) its corresponding BJH adsorption PSDs, and the (c) fwhm of the PSDs of the SBA-15-based materials.

https://doi.org/10.1021/acs.energyfuels.4c03270
Energy Fuels 2024, 38, 23150−23166

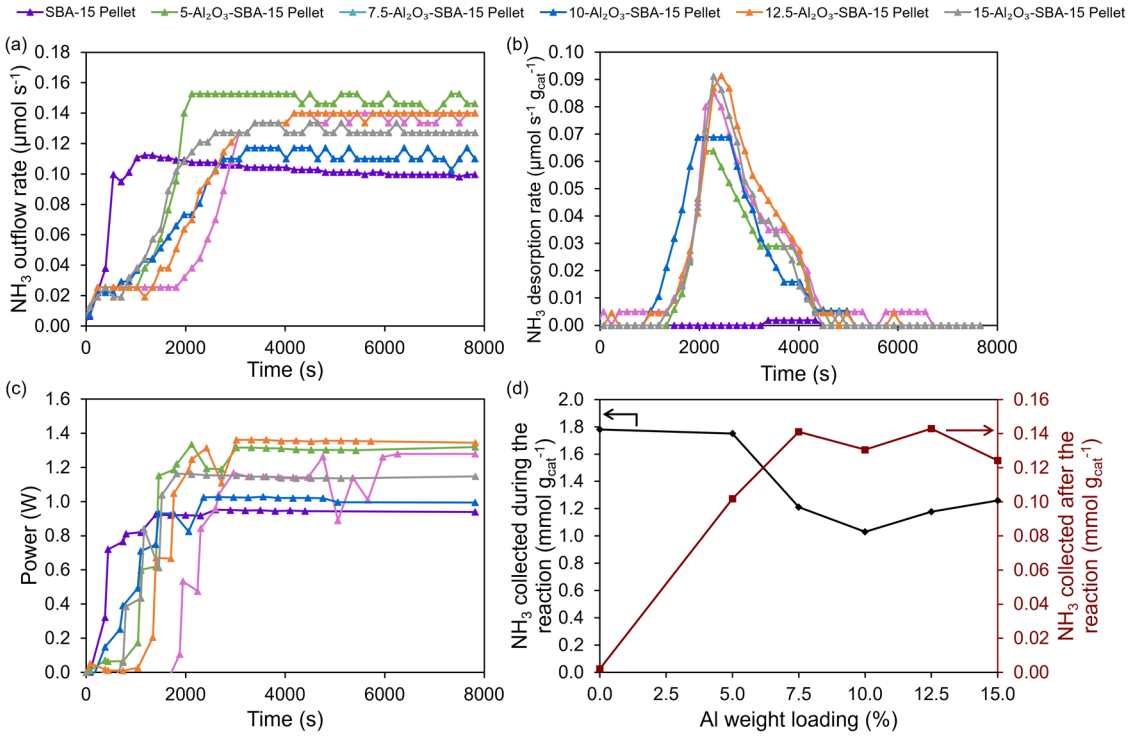

Figure 3. Temporal profiles of (a) absolute NH_3 outflow rates during DBD-assisted reactions at 16 kV, (b) mass-normalized NH_3 desorption rates during a temperature swing after DBD-assisted reaction, and (c) power supplied to generate DBD at 16 kV for NH_3 synthesis in the presence of SBA-15-based materials. (d) NH_3 collected from the reactor during DBD-assisted synthesis and post-reaction TPD (time integral of (a,b) curves, respectively) as a function of Al weight loading. Lines connecting data points are meant to guide the eye. For (a,c), t = 0 represents the DBD ignition.

Reaction Assessment of SBA-15-Based Materials with Varying γ-Al_2O_3 Coating. Previous DBD-assisted NH_3 synthesis work with SBA-15 (in which it was benchmarked with other frameworks like MCM-41 and fumed SiO_2)[47,48] utilized mass-normalized NH_3 outflow rates as different frameworks benefit from fixed bed lengths to keep the bed packing similar across the various porous oxides. However, the fixed packed bed length could lead to significant differences in the mass of catalyst loaded when the porous oxides have very different compositions and structures. In such scenarios, the impact of varying catalyst amounts on the DBD-catalyst synergy, surface reactions, and NH_3 adsorption was scaled via mass normalization, which we utilize in our later comparison of ordered and nonordered porous oxides.

However, we first need to evaluate the performance of the synthesized SBA-15-based materials to determine the effects of varied Al loadings, so the number of catalyst particles loaded in a fixed bed length was maintained. Since Al_2O_3-SBA-15 is a coated composite, the Al incorporation increases the total mass of the loaded material. Al incorporation largely maintains the surface area available for facilitating reactions and NH_3 adsorption, and the exposed surface is likely the primary contributor to the DBD-catalyst synergy, instead of an additive effect of both the γ-Al_2O_3 coat and the SBA-15 surface. As such, mass normalization would unfairly discount the performance of the heavier Al_2O_3-SBA-15 composites as differences in reaction rates are likely due to the different surface identities and not additional surface available. Thus, the absolute NH_3 outflow rate is more relevant for a fair comparison of the SBA-15-based materials. Although it is not used in our analysis here, we also provided their mass-normalized NH_3 outflow rates in Figure S3a.

The aforementioned material characterization indicates that the SBA-15-based materials maintain ordered pores that are evenly coated with γ-Al_2O_3, such that their utilization for DBD-assisted NH_3 production allows us to investigate the effect of varying γ-Al_2O_3 coat thickness on the process (Figure 3). Synthesized in a native powdered form, the SBA-15-based materials were pelletized into larger particles prior to their DBD reactor testing to promote a more homogeneous discharge favorable to NH_3 synthesis.[65] The absolute steady-state NH_3 outflow rate generally appears to be independent of the Al weight loading (as expected from the complete surface coverage indicated in Figure 1), with a slightly lower value for 10-Al_2O_3-SBA-15. Regardless, all of the Al_2O_3-SBA-15 composites have a higher steady-state NH_3 outflow than that of uncoated SBA-15, indicating that the γ-Al_2O_3 coat, via its dielectric properties or surface acid sites, improves DBD-assisted NH_3 production relative to the similar parent SiO_2 framework.

The time taken to reach steady-state NH_3 outflow in the presence of uncoated SBA-15 was much shorter than that for the Al_2O_3-SBA-15 composites (Figure 3a), indicating that the prolonged transient profile of the Al_2O_3-SBA-15 composites is due to the NH_3 uptake by their acid site-functionalized surface. This is further supported by the trend in time taken to reach steady-state NH_3 outflow with respect to the Al loading of the composite, which initially increased with Al loading between 5-Al_2O_3-SBA-15 and 10-Al_2O_3-SBA-15, beyond which it decreased with Al loading between 10-Al_2O_3-SBA-15 and 15-Al_2O_3-SBA-15. The prolonged transient in NH_3 outflow is consistent with the maximum on 10-Al_2O_3-SBA-15 for NH_3 recovered via post-reaction TPD from the SBA-15-based materials (Figure 3b,d).

https://doi.org/10.1021/acs.energyfuels.4c03270
Energy Fuels 2024, 38, 23150−23166

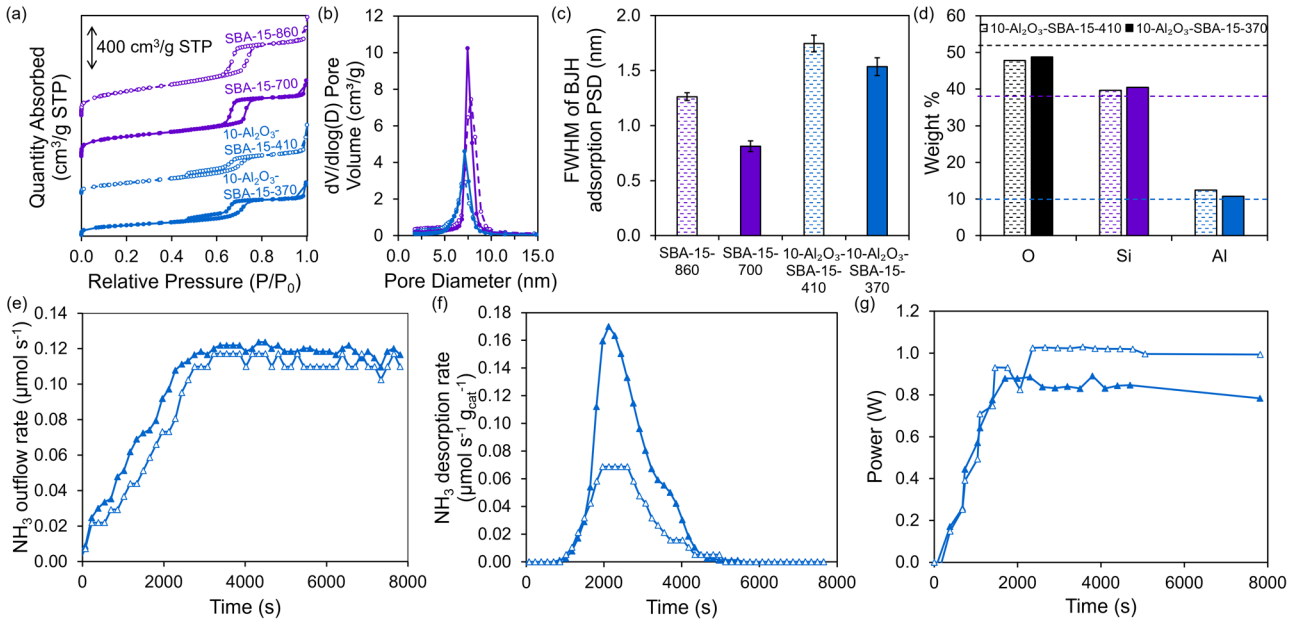

Figure 4. (a) N_2 adsorption−desorption isotherms, (b) its corresponding BJH adsorption PSDs, and the (c) fwhm of the PSDs for uncoated SBA-15-*y* and 10-Al_2O_3-SBA-15-*y* from different synthesis batches, where the suffix *y* is the BET surface area in m^2/g. (d) Elemental composition of the imaged (via SEM/EDX) fresh, as-synthesized 10-Al_2O_3-SBA-15-*y* powders from the different synthesis batches, where the dashed lines indicate target composition. Temporal profiles of (e) absolute NH_3 outflow rates during DBD-assisted synthesis at 16 kV, (f) mass-normalized NH_3 desorption rates during a temperature swing after DBD-assisted synthesis, and (g) power supplied to generate DBD at 16 kV for NH_3 synthesis in the presence of 10-Al_2O_3-SBA-15-*y* materials. For 4e and 4g, t = 0 represents the DBD ignition.

Having characterized the reaction properties via quantification of product NH_3 (both outflow during the DBD-assisted reaction and in situ desorption), the DBD properties were measured using the power supplied to the reactor in the presence of these SBA-15-based materials (Figure 3c). The Lissajous plots (used to determine the power supplied to the DBD) for each SBA-15-based material are provided in Figure S3b; the data collected right before the end of the DBD exposure (i.e., t = 7800 s) was used as a representative time point. The power supplied exhibited an initial increasing trend over time before reaching a plateau on all samples. The initial increase corresponds to the duration over which the power supply was manually increased in response to observed decreases in the applied voltage (so as to indirectly maintain the DBD at 16 kV). The initial transience in the power supplied to the reactor is further explored in a later section on pulsing experiments, where fixing the power supply to its steady-state setting throughout the reaction still resulted in a decrease of the applied voltage during early reaction times; the only difference is that the applied voltage overshot a higher value and then decayed to the steady-state 16 kV. Thus, the initial rise in NH_3 outflow (Figure 3a) and applied voltage for the SBA-15-based materials cannot be circumvented even with a fixed power supply that is left undisturbed. A longer transience was exhibited in the presence of the Al_2O_3-SBA-15 samples than uncoated SBA-15, akin to the NH_3 outflow profile, such that the increase in the power supply required to maintain the same applied voltage during the transient state can similarly be explained by the in situ NH_3 uptake. At DBD start-up, we postulate that the diffusion of species into pores alters local DBD properties, resulting in a lower applied voltage at the same power supplied. Eventually, closer to its equilibrium NH_3 uptake, the excited species are not diffusing out of the bulk DBD significantly; therefore, the applied voltage remains at 16 kV with a fixed power supply, and the power temporal profile plateaus.

The power supplied to the reactor at steady state in the presence of the various Al_2O_3-SBA-15 composites was higher than that of uncoated SBA-15. Within the Al_2O_3-SBA-15 composites, 5-, 7.5- and 12.5-Al_2O_3-SBA-15 exhibited similar steady-state power supplied, which were higher than that of 10- and 15-Al_2O_3-SBA-15. These variations in the steady-state power supplied to the DBD across the different Al loadings differ from the similar steady-state NH_3 outflow rates described earlier, so it is unlikely that the dielectric constant of the material near the surface (and consequently its interaction with the DBD) is different. Furthermore, the Al_2O_3-SBA-15 composites all resulted in a higher power supplied to the DBD than the uncoated SBA-15 sample, which would have depicted the reverse trend if driven by the higher dielectric constant of incorporated γ-Al_2O_3. The higher power supplied to the Al_2O_3-SBA-15 composites is likely because in situ NH_3 uptake by the composites results in greater diffusion of excited species into the pore volume relative to that of uncoated SBA-15, requiring a higher power supplied to maintain the same applied voltage in the bulk DBD, which we elaborate upon in the discussion of Figure 6. However, more DBD characterization is needed to verify this effect.

The similar temporal power profiles in the presence of different SBA-15-based materials suggest that the primary contributor to differences in their NH_3 energy yields is the NH_3 collected during the DBD-assisted reaction and during the post-reaction TPD (obtained from integrating the profiles in Figure 3a,b, respectively, as plotted in Figure 3d). As the time integral of NH_3 outflow, the NH_3 collected during the reaction is (by definition) positively related to the steady-state NH_3 outflow and negatively related to the duration of the transient state. Al_2O_3-SBA-15 composites with a higher Al loading result in lower amounts of NH_3 collected during the

https://doi.org/10.1021/acs.energyfuels.4c03270
Energy Fuels 2024, 38, 23150−23166

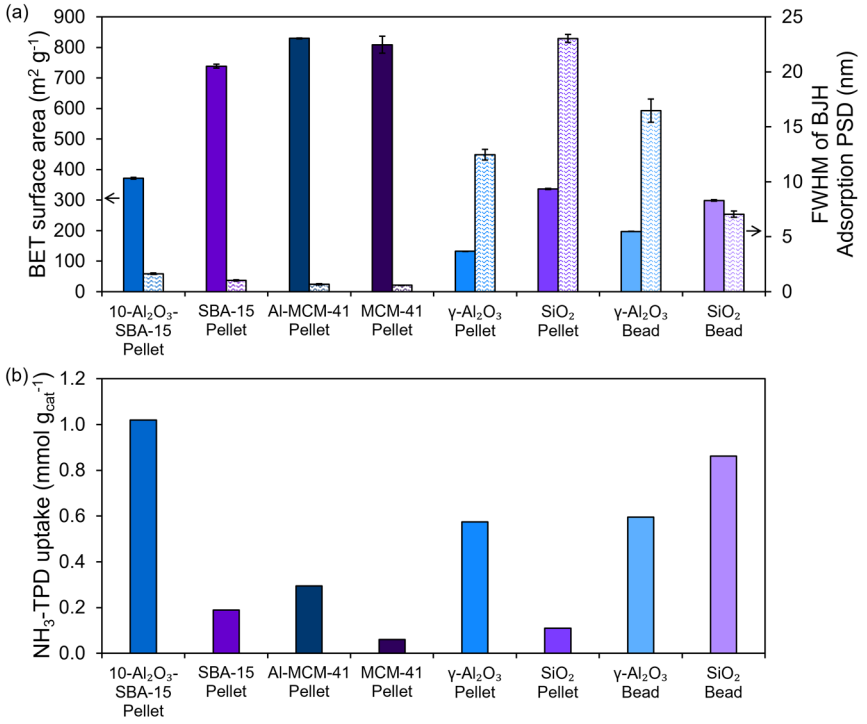

Figure 5. (a) BET surface area and fwhm of BJH adsorption PSD and (b) NH_3 recovered via ex situ TPD (after equilibrium uptake was established at 373 K) for the various fresh porous oxides.

reaction, which is a result of their prolonged transient states. These Al_2O_3-SBA-15 composites exhibit similar NH_3 outflows to one another but varying transient state durations with a maximum at 10-Al_2O_3-SBA-15, as established previously (Figure 3a). In other words, 10-Al_2O_3-SBA-15 corresponds to both the minimum and maximum in the NH_3 collected during the DBD-assisted reaction and post-reaction TPD, respectively, with respect to Al loading. As such, 10-Al_2O_3-SBA-15 was used as the representative weight loading to evaluate the performance of Al_2O_3-SBA-15 relative to that of other porous oxides in subsequent studies.

Effect of SBA-15 Surface Area on Relevant Material and Reaction Properties. At this particular weight loading, we also investigated the effect of the surface area of the parent SBA-15 material. A separate batch of SBA-15 was synthesized following the same protocol but resulted in a lower BET surface area, likely due to slight variations in the amount of viscous P-123 template added. It was coated to form 10-Al_2O_3-SBA-15; the two samples were labeled with a suffix y (i.e., SBA-15-y and 10-Al_2O_3-SBA-15-y), which corresponds to their respective BET surface area in m^2/g (evaluated from N_2 physisorption in Figure 4a). The surface areas of the composites (10-Al_2O_3-SBA-15-370 and 10-Al_2O_3-SBA-15-410) also differ but are more similar than their parent SBA-15 frameworks (SBA-15-700 relative to SBA-15-860). This trend extends to the BJH adsorption PSD (Figure 4b) that had a lesser drop in fwhm (reflecting more ordered pores) for 10-Al_2O_3-SBA-15-370 than 10-Al_2O_3-SBA-15-410 relative to their parents, though the lower fwhm of SBA-15-700 relative to SBA-15-860 (Figure 4c) is likely driving the difference in the 10-Al_2O_3-SBA-15 samples in the first place. The smaller drop in BET surface area in the synthesis of 10-Al_2O_3-SBA-15-370, while preserving the order of the SBA-15 framework, indicates that the even γ-Al_2O_3 coat is likely thinner. Perhaps the lower surface area of SBA-15-700 led to weaker capillary action such that less $Al(NO_3)_3$ solution was taken up into the pores during wetness impregnation, which then formed a thinner γ-Al_2O_3 coating upon calcination to obtain 10-Al_2O_3-SBA-15-370. Regardless, complete siliceous surface coverage and maintaining the pore structure are of greater interest across independent batches of Al_2O_3-SBA-15 than maintaining the thickness of the γ-Al_2O_3 coat.

Fresh, as-synthesized powders of both batches of 10-Al_2O_3-SBA-15 were characterized with EDX-SEM (Figures S4 and S5), with the measured weight loading approximately the same as the target loading (Figure 4d). TEM imaging (also accompanied by EDX analysis) (Figure S6) of fresh, as-synthesized SBA-15-700 and 10-Al_2O_3-SBA-15-370 visually confirms the preservation of the ordered porosity of the SBA-15 framework even with γ-Al_2O_3 incorporation throughout the framework, which would facilitate a high available surface area alongside the acid site functionalization of the pore surface for NH_3 adsorption. Furthermore, uncoated SBA-15-700 and the 10-Al_2O_3-SBA-15-370 composite maintain their ordered porosity after DBD exposure, as shown via TEM imaging (Figure S7), demonstrating that the DBD exposure does not alter the material significantly.

Once characterized in their as-synthesized powder forms, the 10-Al_2O_3-SBA-15-*y* samples were pelletized for testing in a DBD-assisted reactor. The temporal profile of NH_3 outflow during DBD-assisted NH_3 synthesis is similar for both 10-Al_2O_3-SBA-15 samples (Figure 4e), which indicates that the (equilibrated) NH_3 production and in situ NH_3 adsorption are similar across both 10-Al_2O_3-SBA-15 samples at a given reaction time. However, the NH_3 recovered via TPD post-reaction is much greater for 10-Al_2O_3-SBA-15-370 (Figure 4f), which is surprising given its lower surface area. Further characterization is needed to understand the difference in NH_3 uptake; ex situ NH_3-TPD would demonstrate if 10-Al_2O_3-SBA-15-370 has an intrinsic higher acid site density or if its higher

https://doi.org/10.1021/acs.energyfuels.4c03270
Energy Fuels 2024, 38, 23150−23166

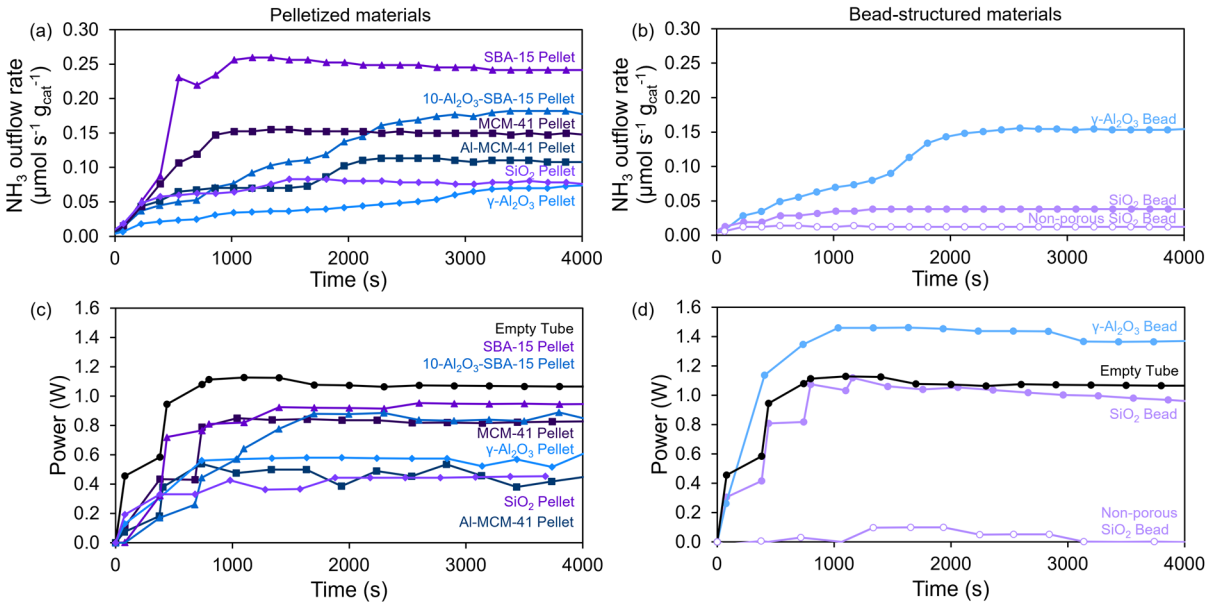

Figure 6. Temporal profile of (a,b) mass-normalized NH_3 outflow rates and (c,d) power supplied during DBD-assisted synthesis at 16 kV in the presence of pelletized and bead-structured porous oxides, respectively, where $t = 0$ represents the DBD ignition, and data is truncated to ∼4000 s.

NH_3 uptake is an artifact of in situ conditions providing greater NH_3 access to the pore volume for adsorption. The material characterization of 10-Al_2O_3-SBA-15-*y* samples and their DBD-assisted NH_3 synthesis activity provide insight into the structural effects on the performance of porous oxides with similar material identity in the reactor. This understanding aids in elucidating the relationship between the DBD-assisted reaction properties and material identity when benchmarking SBA-15-based materials (i.e., SBA-15-700 and 10-Al_2O_3-SBA-15-370, henceforth referred to as SBA-15 and 10-Al_2O_3-SBA-15) against commercial porous oxide packings of varying pore structures and surface functionalities, similarly characterized prereaction.

Comparison of Various Porous Oxides for Single-Stage DBD-Assisted NH_3 Synthesis. Pelletized 10-Al_2O_3-SBA-15 and uncoated SBA-15 were further tested in the DBD-assisted reactor alongside other pelletized ordered materials like MCM-41 and Al-MCM-41, as well as nonordered porous oxides (consisting of similarly pelletized powders or beads), to assess the effect of pore order on DBD-assisted NH_3 synthesis. The pore structures of these various porous oxides were investigated via N_2 physisorption measurements at 77 K, resulting in adsorption−desorption isotherms (Figure S8a) and corresponding BJH adsorption PSDs (Figure S8b,S8c), which verified that pelletized MCM-41-based materials, like the SBA-15-based ones in the previous section have higher BET surface areas and lower fwhm of their BJH adsorption PSD relative to all the nonordered oxides (Figure 5a); though slight disorder was introduced during pelletization of SBA-15, the γ-Al_2O_3 coating resulted in a more mechanically stable material (Figure S8d). The 10-Al_2O_3-SBA-15 pellets were also investigated via N_2 physisorption after testing in the DBD-assisted reactor (Figure S9), demonstrating that its ordered structure was not altered by DBD exposure, in line with the TEM imaging discussed earlier (Figures S6 and S7). Ex situ NH_3-TPD characterizes the potential for NH_3 shielding via adsorption at acid sites in the various porous oxides (Figure S10) as the equilibrium NH_3 uptake at 373 K (Figure 5b), which corresponds to the acid site density. The SiO_2 beads showed an unexpectedly large NH_3 uptake (Figure 5b); however, SEM−EDX revealed significant Al contamination throughout the sample (Figure S11). While we also tested nonporous SiO_2 beads that displayed negligible NH_3 uptake via ex situ TPD (Figure 5b) in the DBD-assisted reactor, this was only used as a qualitative comparison because it is nonporous. For the pelletized porous oxides, both ordered and nonordered Al-based materials exhibited an expected higher acid site density than their SiO_2-based counterparts. 10-Al_2O_3-SBA-15 exhibited the highest NH_3 uptake, while Al-MCM-41 had the lowest NH_3 uptake among the Al-based materials. Moreover, Al-MCM-41 (with Al framework substitution) displayed only one peak in its TPD profile at a relatively high temperature, suggesting a more uniform Al-site, but the TPD profiles of materials containing γ-Al_2O_3 (i.e., Al_2O_3-SBA-15 and the nonordered pellets) appear to have a bimodal distribution with peaks at a lower and higher temperature. NH_3 desorption from Al_2O_3-SBA-15 predominantly corresponds to the lower temperature (∼73%), to a greater extent than the nonordered materials (∼60%) (Figure S10).

The absolute NH_3 outflow rate of DBD-assisted synthesis was higher in the presence of porous oxide beds than in their absence (i.e., empty tube control) (Figure S12a,b), indicative of the synergistic enhancement from the DBD-solid interaction; only the nonporous SiO_2 bead had similar outflow as the empty tube. The materials are separated into plots based on their packed bed configuration (i.e., pelletized or bead-structured), and the empty tube (i.e., no packed bed) data in each plot is normalized by a representative void fraction of its corresponding packed bed configuration, thus accounting for variations in residence time affecting NH_3 outflow rates.

After comparing with the empty tube control, the NH_3 outflow rates of the various porous oxides were compared among one another, and since we are primarily comparing different frameworks, we focus on mass-normalized NH_3 outflow rates for a better representation of the intrinsic performance due to elemental identity and composition changes. The mass-normalized NH_3 outflow rates are again separated into plots for pelletized (Figure 6a) and bead-

https://doi.org/10.1021/acs.energyfuels.4c03270
Energy Fuels 2024, 38, 23150−23166

structured (Figure 6b) porous oxides; the data are not corrected for differences in void fractions as the exact void fraction varies for each porous oxide, and its quantification is challenging for pellet-packed beds. Among the pelletized samples, the SBA-15-based materials had the highest mass-normalized steady-state NH_3 outflow rate, followed by the MCM-41-based materials, and finally, the nonordered porous oxides (Figure 6a). Similar to the discussion on the power supplied to the DBD in the presence of SBA-15-based materials, Figure S13 provides representative Lissajous plots for each porous oxide listed in Figure 6 collected right before the end of the DBD exposure; the data collected right before the end of the DBD exposure (i.e., t = 7800 s) was used as a representative time point. All of the pelletized samples required a lower power supplied to the DBD reactor than the empty tube control to attain the same applied voltage (Figure 6c), which could be indicative of the DBD-support synergy. Combined with their higher steady-state absolute NH_3 outflow rates in Figure S12, we conclude that introducing these porous oxides promotes more energy-efficient synthesis expected from surface catalysis.

Effect of Ordered Pores on NH_3 Outflow Rate and Power Supplied to the DBD. The ordered SiO_2 outperforming the similarly pelletized nonordered SiO_2, and SBA-15 outperforming MCM-41 within the ordered materials, is in line with previously reported results,[47,48] which warrants the testing of the Al-incorporated analogues in our reactor. The paper that studied both SBA-15 and MCM-41 attributed the higher steady-state NH_3 outflow rates measured on SBA-15 than MCM-41,[48] despite their similar hexagonally arranged cylindrical pores, to the interconnected mesopore structure of SBA-15 with micropores in its channel walls[69,70] that is absent in MCM-41.[71] The interconnectivity could facilitate the transportation and storage of NH_3, which they believe affects NH_3 production (and therefore outflow) rate from partial utilization of the internal surface area to facilitate surface reactions, based on another study investigating Ni-loaded MCM-41.[72] While ordered SiO_2 does not have the acid sites for storage of NH_3 via adsorption (consistent with negligible NH_3 recovered during our in situ TPD post-reaction (Figure S14 and 7)), the quicker transport between the mesoporous channels could certainly enhance the accessible internal surface area beyond what was demonstrated for MCM-41, despite the lower total surface area of SBA-15. The similar trend in power supplied to the DBD as the steady-state NH_3 outflow (i.e., SBA-15 > MCM-41 > pelletized nonordered SiO_2; Figure 6c) supports this hypothesis as greater power would be needed needed to maintain the same applied voltage when the excited species in the bulk DBD are being consumed more rapidly for NH_3 production by the greater accessible surface area. It is also possible that it is the changes in the power supplied (i.e., energy available to facilitate the reaction) that was driving the differences in NH_3 production, hence the similar trend in the steady-state power supplied to the DBD and mass-normalized NH_3 outflow rates. The steady-state NH_3 outflow rates in the presence of SBA-15, MCM-41, and nonordered SiO_2 (0.23, 0.14, and 0.077 μmol NH_3 s^{-1} g_{cat}^{-1}, respectively) are all lower than those reported in previous studies on ordered SiO_2 (summarized in Table S2),[47,48] which contextualize our NH_3 outflow rates as within the same order of magnitude as other work in the field. Given differences in applied voltage, discharge gap, void fraction, residence time, etc., across the reactor configurations between studies, it is difficult to assess more rigorous benchmarking. In fact, it is this convolution of different experimental conditions when interpreting NH_3 outflow rates (and energy yields) that motivated our systematic study of DBD-assisted NH_3 synthesis in the presence of common porous oxides with different frameworks and material identities.

The systematic study of ordered SiO_2 frameworks (alongside nonordered porous oxides) within our reactor configuration provides the groundwork for testing their Al-incorporated analogues to elucidate the effect of ordered porosity with a different material identity. The enhancement introduced from ordered porosity extended to the Al-incorporated analogues of ordered SiO_2, given their higher mass-normalized steady-state NH_3 outflow rates than similarly pelletized nonordered γ-Al_2O_3 and 10-Al_2O_3-SBA-15 outperforming Al-MCM-41 within the ordered materials. The mechanism leading to this enhanced performance with ordered porosity may differ; utilization of the internal surface area of the Al-incorporated analogues differs from the parent frameworks as the acid sites allow for NH_3 storage, which plays a role alongside NH_3 transportation within the pores. Thus, despite the blockage of interconnecting micropores of SBA-15 in 10-Al_2O_3-SBA-15 and its lower surface area than Al-MCM-41, its greater NH_3 storage demonstrated via in situ recovery (Figure S14) and ex situ measurements (Figure 5b) could lead to diffusion of excited species deeper into the pore volume and a greater shift of the equilibrium-limited reaction in the forward direction. This could also explain the deviation in the trend of the power supplied to the DBD reactor from that of mass-normalized steady-state NH_3 outflow rates. The power supplied was highest in the presence of 10-Al_2O_3-SBA-15, which also yields the highest steady-state NH_3 outflow, followed by pelletized nonordered γ-Al_2O_3 then Al-MCM-41, even though nonordered γ-Al_2O_3 had a lower steady-state NH_3 outflow rate. Nonordered γ-Al_2O_3 has a greater capacity for NH_3 storage as seen in ex situ measurements (Figure 5b) and the slower rise to steady-state NH_3 outflow measured in its presence (Figure 6a). However, similar in situ NH_3 uptake as quantified by the post-reaction TPD recovery (Figures S14 and 7) likely means that diffusion of active species into the pore volume of pelletized nonordered γ-Al_2O_3 and Al-MCM-41 was comparable, which translates to regenerating a similar density of excited species in the bulk DBD to maintain the applied voltage. The similar extent of regeneration likely requires a similar power supplied to the DBD, as observed in the steady-state power supplied in the presence of pelletized nonordered γ-Al_2O_3 and Al-MCM-41 (Figure 6c). The higher mass-normalized steady-state NH_3 outflow of Al-MCM-41 suggests that despite the similar NH_3 uptake, more of the internal surface area of Al-MCM-41 was utilized for DBD-assisted synthesis, which is consistent with the isolate, dilute nature of acid sites in Al-MCM-41; therefore, similar NH_3 uptake via adsorption on acid sites would naturally involve more of the internal surface area. In short, the benefits observed with ordered porosity in Al-incorporated structures arise from a combination of enhanced NH_3 transportation within the ordered framework and NH_3 storage from Al incorporation.

Effect of Material Identity (Al-Based vs SiO_2) and Packing (Pellet versus Bead) on NH_3 Outflow Rate and Power Supplied to the DBD. While the trend in mass-normalized steady-state NH_3 outflow rates for the Al-incorporated analogues follows that of their parent ordered SiO_2 frameworks, it would be unfair to attribute this

https://doi.org/10.1021/acs.energyfuels.4c03270
Energy Fuels 2024, 38, 23150−23166

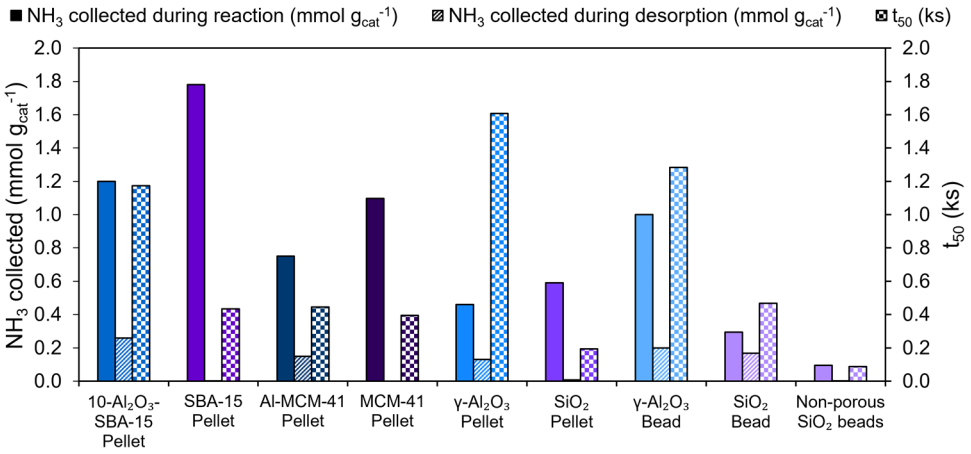

Figure 7. Plot of NH_3 recovered from the reactor during DBD-assisted synthesis at 16 kV (solid) and post-reaction TPD (striped) as well as the t_{50} (time taken to reach 50% of steady-state NH_3 outflow during the DBD-assisted reaction; checkered) in the presence of different porous oxides.

performance solely to the framework when the type of Al incorporation is different. Thus, we gain insight into the effect of the Al incorporation technique by comparing the steady-state NH_3 outflow rates of the Al-incorporated ordered SiO_2 as the difference from their respective parent SiO_2 framework. As mentioned above, we compare the absolute NH_3 outflow rate to assess the performance of similarly structured frameworks such as Al_2O_3-SBA-15 and uncoated SBA-15, and this also holds for comparing Al-MCM-41 to MCM-41. We refer to the absolute NH_3 outflow rates in Figure S12, where 10-Al_2O_3-SBA-15 exhibits similar steady-state NH_3 outflow as SBA-15, but Al-MCM-41 exhibits a lower steady-state NH_3 outflow than MCM-41. The trend in power supplied to the DBD is similar, where 10-Al_2O_3-SBA-15 and SBA-15 demonstrated similar steady-state powers, but Al-MCM-41 had a lower power supplied than MCM-41 (Figure 6c). Again, the different amounts of power supplied to the system may be driving the different NH_3 outflow rates observed. Both parent SiO_2 frameworks show negligible NH_3 uptake both in situ (Figures S14 and 7) and ex situ (Figure 5b); so comparing the Al-incorporated analogues directly, it is evident that 10-Al_2O_3-SBA-15 has greater NH_3 storage. However, as mentioned earlier, 10-Al_2O_3-SBA-15 requires greater power supplied to the DBD to maintain the same applied voltage as Al-MCM-41, which has a competing negative effect on the NH_3 energy yield, which will be addressed in more detail in the next section.

The comparison between parent ordered SiO_2 and Al-incorporated analogues can be extended to the nonordered porous oxides (both pelletized powders and beads) to elucidate general trends. While the relative steady-state NH_3 outflow varied greatly (i.e., 10-Al_2O_3-SBA-15 ≈ SBA-15, Al-MCM-41 < MCM-41, γ-Al_2O_3 pellet ≈ SiO_2 pellet, γ-Al_2O_3 bead > SiO_2 bead), it matched the trend in power supplied to the DBD, indicating that, perhaps, the difference in material identity affects the DBD-support synergy reflected in the power supplied to the reactor, and it is those changes in the power supplied (i.e., energy available to facilitate the reaction) that drive the differences in NH_3 production. Despite the differences in the relative steady-state NH_3 outflow, all Al-based materials took much longer to establish that steady-state outflow, as quantified by the t_{50} values in Figure 7. The prolonged transience for each Al-based material corresponds to its in situ NH_3 uptake that is generally absent in the SiO_2 materials (Figures S14 and 7), with the exception of the SiO_2 beads due to its Al contamination (Figure S11), as discussed earlier with regard to its significant ex situ measurement (Figure 5b). The NH_3 recovered from Al-based materials would be beneficial in an overall energy yield comparison to their SiO_2 counterparts, but even with a higher or similar steady-state NH_3 outflow, they can be disadvantaged by the prolonged transient state collecting less NH_3 over a reaction of fixed duration (Figure 7), thus their relative overall energy yields need more careful consideration and are explored in the next section.

For the bead-structured oxides, the SiO_2 beads had the lowest mass-normalized steady-state NH_3 outflow, lower than that of all the pelletized materials, while the γ-Al_2O_3 beads had a higher mass-normalized steady-state NH_3 outflow, similar to that of the MCM-41-based materials (Figure 6b). The SiO_2 and γ-Al_2O_3 beads had similar and greater steady-state power supplied to the DBD relative to the empty tube control, respectively, which does not necessarily negate the notion of DBD-support synergy but suggests a stronger competing effect on the power supplied to the DBD. High in situ NH_3 uptake would necessitate more power supplied to the DBD at fixed applied voltages, given strong diffusional gradients within the pore volume and promotion of the forward NH_3 production reaction in the equilibrium-limited synthesis. Thus, high NH_3 uptake during the reaction would counteract the reduced DBD power required from synergistic support interactions, especially for the bead-structured porous oxides, which have demonstrated significant NH_3 uptake both in situ (Figures S14 and 7) and ex situ (Figure 5b)). The higher steady-state power supplied to the γ-Al_2O_3 beads relative to the SiO_2 beads could potentially drive the similar trend in mass-normalized steady-state NH_3 outflow rate. The nonporous SiO_2 beads showed very narrow Lissajous profiles that translated to a negligible (calculated) power supplied to the DBD-assisted reactor, but we believe that the irregular Lissajous plots reflect the disintegration of the beads, which were discolored and fused together after the DBD-assisted reaction with visible etching on the quartz tube walls. Given the instability of this system and unreliable power supplied quantification, it is not discussed in subsequent energy yield comparisons.

Both beads also exhibit greater DBD power than all the pelletized porous oxides, likely due to inhibition of DBD generation (i.e., higher breakdown voltage) with smaller

https://doi.org/10.1021/acs.energyfuels.4c03270
Energy Fuels 2024, 38, 23150−23166

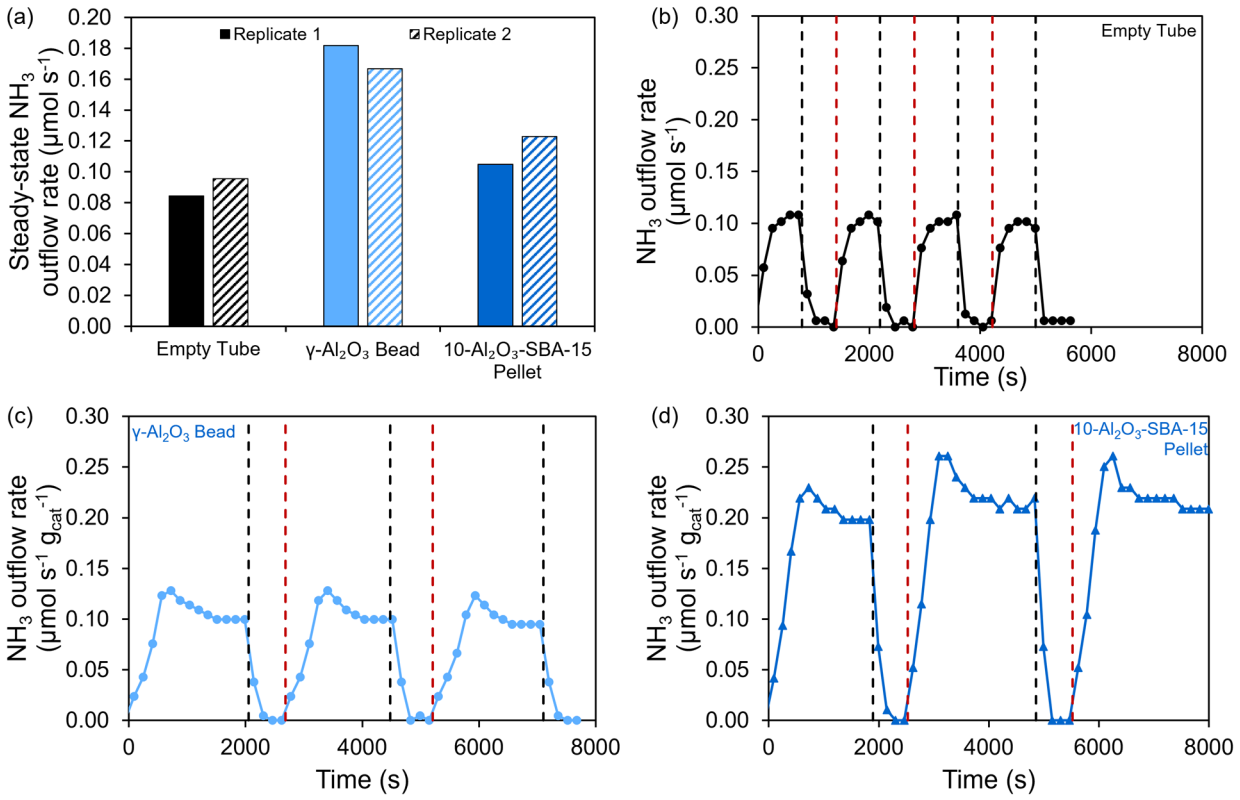

Figure 8. (a) Steady-state NH_3 outflow rates across replicates (over the typical reaction duration of 8000 s) in the presence and absence of different porous oxides. Temporal profiles of NH_3 outflow (b) without a packed bed (i.e., empty tube control), (c) in the presence of Al_2O_3 beads, and (d) in the presence of 10-Al_2O_3-SBA-15 pellets under pulsed DBD exposure at constant power after a replicate experiment. The red dashed lines represent when the DBD was ignited, and the black dash lines represent when the DBD was extinguished.

interparticle voids in a pellet bed packing structure, hence a partial discharge.[65] The effect of the packed bed configuration on the mass-normalized steady-state NH_3 outflow is unclear, as a comparison of the nonordered porous oxides reveals that the bead-structure is preferred for the γ-Al_2O_3 materials, but the pelletized powder is preferred for the SiO_2 materials. This could be due to the unaccounted difference in residence times in the respective packed bed configuration, where the closely packed pellets with a smaller void fraction probably result in limited time for the DBD-assisted reaction that negatively impacts their steady-state NH_3 production and outflow rates. However, it is promising that the ordered materials have similar (i.e., MCM-41-based materials) or greater (i.e., SBA-15-based materials) mass-normalized steady-state NH_3 outflow rates relative to those of typical porous oxide beads. Combined with the lower power supplied to the DBD in the presence of ordered porous oxides, they likely have competitive energy yields benchmarked against current metal catalyst supports, paving the way for their direct use as metal catalyst supports with high NH_3 energy yields, which will be discussed in the next section.

Reproducibility of NH_3 Outflow and Transience Dependence on Material and Plasma History. This energy yield is a meaningful descriptor only if the measured NH_3 outflow is reproducible, especially for Al-based materials with significant NH_3 uptake. Thus, we ran independent replicates for 10-Al_2O_3-SBA-15 and γ-Al_2O_3 beads, chosen to demonstrate different packed bed configurations and material identity (i.e., Al-incorporated vs γ-Al_2O_3) as well as an empty tube configuration as a control. The steady-state NH_3 outflows in the replicate runs were consistent with the original run of the control and the packed materials (Figure 8a), indicating the reproducibility of the DBD-assisted reactor performance.

Even though replicates remained consistent for candidate samples, they do not address the initial transient observed for runs (Figure 6a). While the transient was prolonged in the presence of Al-based materials, it was still present (to a smaller extent) in the presence of SiO_2 materials (as shown by the t_{50} values in Figure 7). Even the empty tube control exhibited a brief transience in the NH_3 outflow rate, with a t_{50} value of 160 s, which would be consistent with some "plasma conditioning" of the dielectric tube wall when the high potential difference is first applied for the DBD to equilibrate. Thus, the slightly larger t_{50} of SiO_2 materials (Figure 7) is likely due to the equilibration of the DBD-support interaction alongside the equilibration with the tube wall. The equilibration of the DBD-support interaction probably also encompasses the utilization of the internal surface area of the SiO_2 materials, as the t_{50} values trend with the accessibility of the pore volume and internal surface area. Pelletized nonordered SiO_2 has the lowest t_{50} value, below that of the high surface area, ordered SiO_2 materials. Within the ordered materials, SBA-15 (with interconnecting micropores enabling greater access to the mesoporous channels) has a slightly larger t_{50} value than MCM-41.

We also wanted to understand if the prolonged transience observed with these Al_3-based materials is purely related to NH_3 uptake by the fresh porous oxide packing prior to steady-state being established or if there is an intrinsic material property leading to the transience even after DBD exposure

https://doi.org/10.1021/acs.energyfuels.4c03270
Energy Fuels 2024, 38, 23150−23166

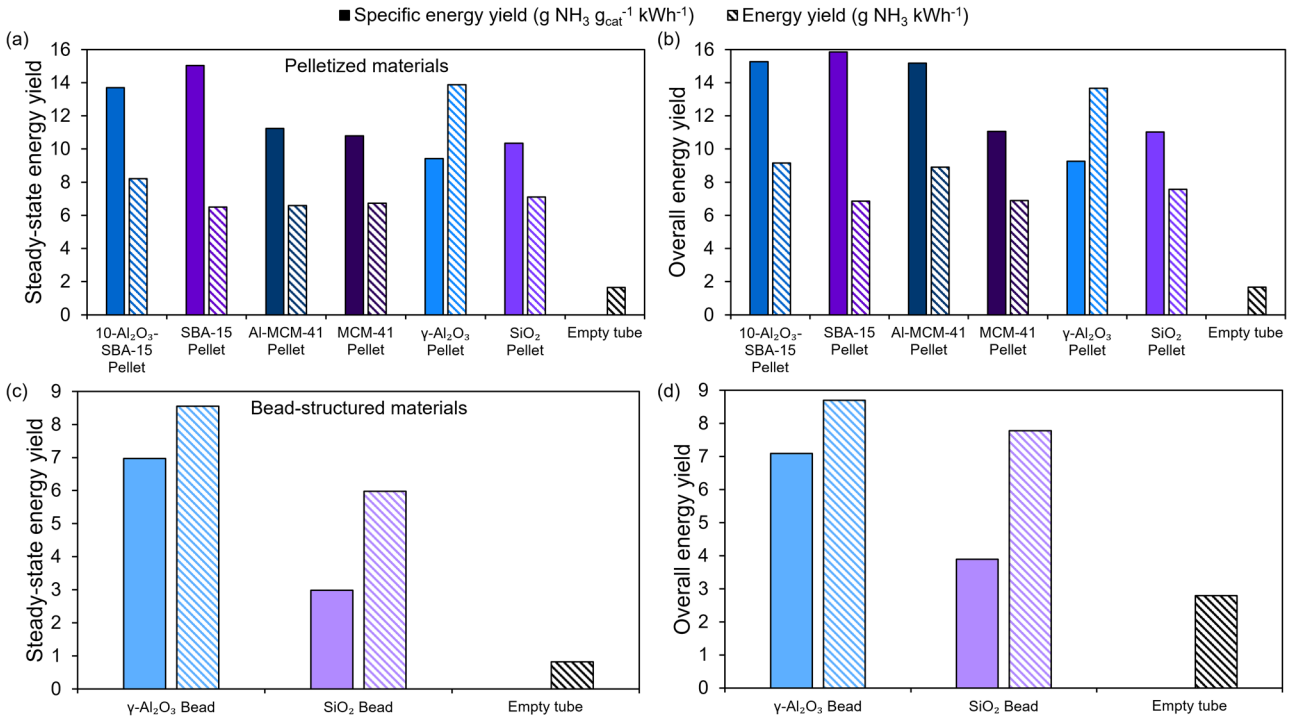

Figure 9. Steady-state and overall (reaction duration = 8000 s) NH_3 energy yields of the DBD-assisted reactor at 16 kV in the presence of (a,b) pelletized and (c,d) bead-structured porous oxides, respectively, with an empty tube (i.e., no packed bed) control.

and established steady-state NH_3 outflow. Thus, we performed pulsing experiments after a typical experimental run in which steady-state NH_3 outflow was established, as outlined in the Experimental Section, on 10-Al_2O_3-SBA-15, γ-Al_2O_3 beads, and the empty tube control. At the end of the replicate run, when the NH_3 outflow was still at steady state, the DBD was shut off; the empty tube configuration showed a similar rise to steady-state NH_3 outflow rate as the initial transient state without any plasma exposure (Figure 8b), which demonstrates that the "plasma conditioning" and equilibration of the dielectric tube wall do not vary regardless of previous DBD exposure/cycling. During the DBD pulsing, the γ-Al_2O_3 beads and 10-Al_2O_3-SBA-15 pellets both exhibited a quick initial rise to the known, eventual steady-state NH_3 outflow rate but did not attain steady-state at that point. Instead of plateauing, the NH_3 outflow rate proceeded to overshoot to a higher rate, after which it decayed back to and stabilized at the steady-state NH_3 outflow rate. For both γ-Al_2O_3 beads and 10-Al_2O_3-SBA-15 pellets, the initial rise to steady-state NH_3 outflow rate (prior to the overshoot) was on a similar time scale as the empty tube configuration (Figure 8c and d, respectively), as opposed to their initial prolonged transient state prior to any DBD exposure (Figure 6a and b, respectively). The absence of morphological changes in the porous oxides post-DBD exposure rules out structural changes to the material that might shorten the transient duration. Thus, it further confirms that the initial prolonged transient state is likely due to NH_3 uptake by these acid-functionalized materials, and that once these materials are saturated with NH_3 (thus reaching steady-state NH_3 outflow), subsequent pulsing results in a shorter rise to initially hit steady-state NH_3 outflow values, similar to the transient duration of the empty tube control, likely due to equilibration of the DBD and dielectric tube wall.

Once the NH_3 outflow rate initially overshot the expected steady-state value in the presence of γ-Al_2O_3 beads and 10-Al_2O_3-SBA-15 pellets, it slowly decayed back to that steady-state value. Unlike the time taken to first reach steady-state NH_3 outflow, this full duration of their transient profile is consistent with the transience in the DBD properties observed in the first 15−20 min during the original run of experiments. For the former (i.e., pulsing experiments), a fixed power was supplied corresponding to 16 kV at steady-state, and we observed the applied voltage overshoot past 16 kV initially before decaying back over time, which is likely the driving force for the similar trend in the NH_3 outflow rate. For the latter (i.e., original run of experiments), the power supplied was adjusted based on the instantaneous applied voltage (as outlined in the Experimental Section), where we observed the applied voltage decay with time from 16 kV during the initial plasma exposure (15−20 min), and additional power was concomitantly supplied to counteract it until it stabilized at 16 kV. The transient profile of the pulses is longer for 10-Al_2O_3-SBA-15 pellets than for γ-Al_2O_3 beads, which could be related to the different packed bed configurations or other factors, but further studies would be necessary to fully understand this transient profile of NH_3 outflow rate, which is a mix of the DBD-support and reaction equilibration.

While the spent porous oxides were not recycled in the DBD-assisted reactor for stability testing, the convergence to a steady-state NH_3 outflow rate that is similar across independent replicates and consecutive pulses in the representative packed bed configurations also suggests the stability of the porous oxides under DBD exposure, corroborating the TEM data (Figures S6 and S7) and N_2 physisorption data (Figure S9) presented earlier. We expect this stability to hold for other ordered materials and nonordered materials with simpler structures, especially given that the steady-state NH_3 outflow was maintained for over an hour in the presence of all the porous oxide packed beds

https://doi.org/10.1021/acs.energyfuels.4c03270
Energy Fuels 2024, 38, 23150−23166

(Figure 6a depicts truncated data that omits this extended steady-state for clarity).

Energy Yields of DBD-Assisted NH_3 Production in the Presence of Various Porous Oxides. Having established the reproducibility of NH_3 outflow rates across independent replicates and an initial study into the causes and contribution to its transient profiles, we shifted our focus to the NH_3 energy yield, a key performance indicator of DBD-assisted NH_3 synthesis, to compare the various porous oxides because it is the amount of desired NH_3 product obtained per unit energy expended. It accounts for both the NH_3 outflow rates (Figure 6a and b) and power supplied to the reactor (Figure 6c and d) in the steady-state NH_3 yield, with the added consideration of NH_3 recovered post-reaction via TPD (Figures S14 and 7) in the overall NH_3 yield, which are calculated using the procedure outlined in the Experimental Section. The overall energy yield is of greater interest as accounting for the shielded NH_3 improves the energy yield as desired, which we aim to harness with the Al-functionalization of high-performing parent ordered SiO_2. However, the relative overall energy yields vary not only with the material identity but also with the reaction duration chosen to evaluate it over. Relative steady-state energy yields are intrinsic to the packing material, especially since their performance is evaluated at a fixed applied voltage with different power supplied to the DBD with potential contribution to the NH_3 outflow rates. Normalizing the NH_3 outflow rate with the power supplied in the steady-state energy yield allows us to approximate the NH_3 production differences unrelated to power effects, so both metrics are utilized in comparing the different porous oxides.

Here, we evaluated the NH_3 energy yield on a steady-state basis (Figure 9a and c) and an overall basis (Figure 9b and d) in the presence of the pelletized and bead-structured porous oxides, respectively. The use of mass-normalized or absolute quantities follows what was established in the discussion of the relative NH_3 outflow rates. The energy yields are also not adjusted for varying residence times of the different packed beds, again an important caveat when comparing the different porous oxides, especially across different packed bed configurations. The NH_3 energy yield of the empty tube control in each plot is adjusted by a representative void fraction for the corresponding packed bed configuration (Figure 9) and demonstrates that the introduction of the porous oxide packed bed significantly improves the energy yield in all of our experiments.

Steady-State and Overall NH_3 Energy Yields of Ordered Materials. Comparing SBA-15 and MCM-41 elucidates the effect of the ordered SiO_2 framework on the NH_3 energy yield, where MCM-41 exhibited a lower mass-normalized steady-state energy yield than SBA-15 (Figure 9a). As established earlier, we suspect that there is less effective utilization of the MCM-41 internal surface area that leads to lower NH_3 outflows and power supplied, which have counteracting effects on the steady-state energy yield. The detrimental effect of lower NH_3 outflow clearly had a larger impact, so the steady-state energy yield of MCM-41 is lower than that of SBA-15. With minimal NH_3 evolved post-reaction, a similar trend held true for the mass-normalized overall energy yield between the two ordered SiO_2 frameworks (Figure 9b). The pelletized nonordered SiO_2 had a similar mass-normalized steady-state and overall energy yield as MCM-41 (Figure 9a,b), indicating that the counteracting lower NH_3 outflow and power supplied to the reactor for nonordered SiO_2 pellets compared to MCM-41 balanced out in the energy yield calculation. Thus, simply introducing ordered porosity does not necessarily increase the NH_3 energy yields. Again, the studies on DBD-assisted NH_3 production with ordered and nonordered SiO_2 summarized in Table S2 provide context for the NH_3 energy yields we obtained, which were greater than the values reported in one study[48] but lower than the values reported in the other,[47] but in both cases within an order of magnitude of the reported values. Again, the differences in the reactor configurations and operation can greatly affect the NH_3 energy yield, necessitating our systematic study of common porous oxides, especially prior to evaluating novel Al-incorporated analogues of the ordered SiO_2. For these analogues, 10-Al_2O_3-SBA-15 reported the highest mass-normalized steady-state energy yield, followed by the Al-MCM-41 and pelletized γ-Al_2O_3 powder, which follows the trend in steady-state NH_3 outflow that clearly had a stronger impact than the opposing trend in power supplied to the DBD. However, Al-MCM-41 exhibits a similar mass-normalized overall energy yield as 10-Al_2O_3-SBA-15, so accounting for recovered NH_3 can strongly affect the energy yield in the presence of a given porous oxide material.

Contrasting the ordered materials also provides insight into the effect of the type of Al incorporation within the ordered SiO_2 on the NH_3 energy yield. 10-Al_2O_3-SBA-15 exhibited a higher absolute steady-state energy yield than SBA-15, while MCM-41 and Al-MCM-41 performed similarly, in line with the trends in NH_3 outflow, and suggesting that the γ-Al_2O_3 coat more effectively influences the DBD-support synergy and/or has a greater density of acid sites than achieved by the Al framework substitution. Both Al-incorporated analogues demonstrated NH_3 recovery, which leads to their higher overall energy yield relative to their respective parent SiO_2 framework. 10-Al_2O_3-SBA-15 demonstrated a greater increase in overall energy yield relative to SBA-15 compared to that of Al-MCM-41 relative to MCM-41, which is in line with the greater NH_3 recovery observed for 10-Al_2O_3-SBA-15. Al incorporation via a γ-Al_2O_3 coat appears to be more effective in NH_3 uptake and steady-state NH_3 outflow than Al incorporation via framework substitution, which could be due to multiple reasons but most likely due to a greater acid site density on the γ-Al_2O_3 coat than isolated Bronsted acid sites in Al-MCM-41.

Effect of Packed Bed Configuration and Material Identity (i.e., Al-Based vs SiO_2) on Steady-State and Overall NH_3 Energy Yields. While the nonordered beads and pelletized powders were originally tested in our DBD-assisted reactor to provide systematically studied benchmarks for the ordered materials, as discussed above, their internal comparison also approximates the reactor- and reaction-specific packed bed configuration effect of similar materials on the NH_3 energy yields. The nonordered pellets had higher mass-normalized steady-state and overall energy yields than the beads, even without correcting for the disadvantageous lower residence time. The conflicting trends in NH_3 outflow rates (which varied with the porous oxide identity) were masked by the stronger trends in power supplied to the DBD-assisted reactor, which were greater for the beads than for the pellets regardless of material identity. Lastly, the effect of the porous oxide identity on the NH_3 energy yield was investigated by comparing the Al-based materials with their SiO_2 counterparts, all of which exhibited an increase in the overall energy yield, as expected since the Al-based materials demonstrated NH_3

https://doi.org/10.1021/acs.energyfuels.4c03270
Energy Fuels 2024, 38, 23150−23166

recovery post-reaction unlike the SiO_2 materials. The Al-based materials were solidified as the preferred porous oxide packings, like previously reported results for the steady-state NH_3 outflow.

Ultimately, our systematic study of a suite of porous oxides allowed us to quantify their energy yield contributions as potential metal supports within an identical setup, as a function of their material properties and reactor configuration. We extended previous results for ordered SiO_2 to their Al-incorporated analogues, investigated preferred types of Al incorporation, demonstrated that Al-based materials generally allow for NH_3 recovery to boost the overall energy yield, and lastly, discussed the strong influence of DBD power trends biased energy yields toward pellet-packed bed configurations, despite their complicated effects on the NH_3 outflow rates.The ordered materials (particularly the synthesized SBA-15-based materials) exhibited promising NH_3 energy yields, supporting future work in acid-site functionalization of ordered supports and harnessing NH_3 shielding for higher energy yields.

CONCLUSIONS

We investigated a suite of ordered and nonordered porous oxides (common metal catalyst support materials) in our DBD-assisted reactor to probe their NH_3 energy yield contribution. We studied SBA-15 and MCM-41, which are previously explored ordered SiO_2 frameworks, and benchmarked them against similarly pelletized nonordered powder to verify literature results about the higher performance of ordered materials. We also compared them to typical bead-structured porous oxides to show their superior energy yield, benefiting from the lower power supplied trends for pellet-packed bed configurations. We demonstrated that for the nonordered porous oxides, the γ-Al_2O_3 materials have a higher overall yield accounting for the shielded NH_3. As such, we explored Al-incorporated analogues of the ordered SiO_2 frameworks using different incorporation techniques, commercial Al-MCM-41 with isolated acid sites at framework substitution points and in-house-synthesized γ-Al_2O_3-coated SBA-15 (Al_2O_3-SBA-15). We synthesized γ-Al_2O_3-SBA-15 with different Al weight loadings and evaluated the various composites in the DBD-assisted reactor to determine whether 10-Al_2O_3-SBA-15 shields the most NH_3. It demonstrated similar high energy yields as SBA-15, but Al-MCM-41 had a similar overall energy yield when accounting for recovered NH_3. Both analogues outperformed the nonordered beads and pellets, extending the finding for ordered SiO_2 to its Al-incorporated analogues, with potential direct applications as metal catalyst supports for various DBD plasma-assisted reactions.

ASSOCIATED CONTENT

Supporting Information

The Supporting Information is available free of charge at https://pubs.acs.org/doi/10.1021/acs.energyfuels.4c03270.

Additional characterization data of the materials (full FTIR spectra, SEM/TEM images with EDX, N_2 physisorption and NH_3-TPD) and reaction (outflow and desorption) NH_3 reactor data and Lissajous plots for the power curves (PDF)

AUTHOR INFORMATION

Corresponding Author

Michele L. Sarazen − *Department of Chemical and Biological Engineering, Princeton University, Princeton, New Jersey 08544, United States;* orcid.org/0000-0002-5732-7130; Email: msarazen@princeton.edu

Authors

Sonia E. Arumuganainar − *Department of Chemical and Biological Engineering, Princeton University, Princeton, New Jersey 08544, United States;* orcid.org/0009-0004-6588-9725

Stavroula Sartzetakis − *Department of Chemical and Biological Engineering, Princeton University, Princeton, New Jersey 08544, United States;* orcid.org/0009-0002-2607-4078

Cole W. Hullfish − *Department of Chemical and Biological Engineering, Princeton University, Princeton, New Jersey 08544, United States;* orcid.org/0000-0001-6804-0517

Bruce E. Koel − *Department of Chemical and Biological Engineering, Princeton University, Princeton, New Jersey 08544, United States;* orcid.org/0000-0002-0032-4991

Complete contact information is available at: https://pubs.acs.org/10.1021/acs.energyfuels.4c03270

Notes

The authors declare no competing financial interest.

ACKNOWLEDGMENTS

This work was supported by the U.S. Department of Energy, Office of Science, Office of Fusion Energy Sciences under award number DE-SC0020233 and by the U.S. Department of Energy, Office of Science Energy Earthshot Initiative as part of the Center for the Science of Plasma-Enhanced Hydrogen Production at Princeton Plasma Physics Laboratory under contract #DEAC0209CH11466. S.E.A. acknowledges partial support by the Program in Plasma Science and Technology (PPST) at Princeton University. The authors acknowledge the use of Princeton's Imaging and Analysis Center, which is partially supported through the Princeton Center for Complex Materials (PCCM), a National Science Foundation (NSF)-MRSEC program (DMR2011750). We would also like to thank previous members of the Koel lab (Dr. David Caron, Dr. Zhe Chen, and Dr. Surabhi Jaiswal) working on similar projects for their aid in designing the DBD setup and interpreting the collected data.

REFERENCES

(1) Foster, S. L.; Bakovic, S. I. P.; Duda, R. D.; Maheshwari, S.; Milton, R. D.; Minteer, S. D.; Janik, M. J.; Renner, J. N.; Greenlee, L. F. Catalysts for Nitrogen Reduction to Ammonia. *Nat. Catal.* **2018**, *1* (7), 490−500.

(2) International Energy Agency *Ammonia Technology Roadmap*: Paris, 2021.

(3) Pattabathula, V.; Richardson, J. *Introduction to Ammonia Production*; CEP Magazine, 2016; . September .

(4) Jiao, F.; Xu, B. Electrochemical Ammonia Synthesis and Ammonia Fuel Cells. *Adv. Mater.* **2019**, *31* (31), 1805173.

(5) MacFarlane, D. R.; Cherepanov, P. V.; Choi, J.; Suryanto, B. H. R.; Hodgetts, R. Y.; Bakker, J. M.; Ferrero Vallana, F. M.; Simonov, A. N. A Roadmap to the Ammonia Economy. *Joule* **2020**, *4* (6), 1186−1205.

(6) Guo, J.; Chen, P. Catalyst NH3 as an Energy Carrier. *Chem.* **2017**, *3* (5), 709−712.

(7) Lan, R.; Irvine, J. T. S.; Tao, S. Ammonia and Related Chemicals as Potential Indirect Hydrogen Storage Materials. *Int. J. Hydrogen Energy* **2012**, *37*, 1482−1494.
(8) Klerke, A.; Christensen, C. H.; Nørskov, J. K.; Vegge, T. Ammonia for Hydrogen Storage: Challenges and Opportunities. *J. Mater. Chem.* **2008**, *18* (20), 2304−2310.
(9) Rouwenhorst, K. H. R.; Lefferts, L. Feasibility Study of Plasma-Catalytic Ammonia Synthesis for Energy Storage Applications. *Catalysts* **2020**, *10* (9), 999.
(10) Bogaerts, A.; Tu, X.; Whitehead, J. C.; Centi, G.; Lefferts, L.; Guaitella, O.; Azzolina-Jury, F.; Kim, H.-H.; Murphy, A. B.; Schneider, W. F.; Nozaki, T.; Hicks, J. C.; Rousseau, A.; Thevenet, F.; Khacef, A.; Carreon, M. The 2020 Plasma Catalysis Roadmap. *J. Phys. D Appl. Phys.* **2020**, *53* (44), 443001.
(11) Schiffer, Z. J.; Manthiram, K. Electrification and Decarbonization of the Chemical Industry. *Joule* **2017**, *1* (1), 10−14.
(12) Mehta, P.; Barboun, P.; Go, D. B.; Hicks, J. C.; Schneider, W. F. Catalysis Enabled by Plasma Activation of Strong Chemical Bonds: A Review. *ACS Energy Lett.* **2019**, *4* (5), 1115−1133.
(13) Zhang, J.; Li, X.; Zheng, J.; Du, M.; Wu, X.; Song, J.; Cheng, C.; Li, T.; Yang, W. Non-Thermal Plasma-Assisted Ammonia Production: A Review. *Energy Convers. Manag.* **2023**, *293*, 117482.
(14) Mizushima, T.; Matsumoto, K.; Sugoh, J.; Ohkita, H.; Kakuta, N. Tubular Membrane-like Catalyst for Reactor with Dielectric-Barrier-Discharge Plasma and Its Performance in Ammonia Synthesis. *Appl. Catal., A* **2004**, *265* (1), 53−59.
(15) Mindong, B.; Zhitao, Z.; Xiyao, B.; Mindi, B.; Wang, N. Plasma Synthesis of Ammonia with a Microgap Dielectric Barrier Discharge at Ambient Pressure. *IEEE Trans. Plasma Sci.* **2003**, *31* (6), 1285−1291.
(16) Nakajima, J.; Sekiguchi, H. Synthesis of Ammonia Using Microwave Discharge at Atmospheric Pressure. *Thin Solid Films* **2008**, *516* (13), 4446−4451.
(17) Kim, M.; Biswas, S.; Nava, G.; Wong, B. M.; Mangolini, L. Reduced Energy Cost of Ammonia Synthesis Via RF Plasma Pulsing. *ACS Sustain. Chem. Eng.* **2022**, *10* (46), 15135−15147.
(18) Hong, J.; Prawer, S.; Murphy, A. B. Production of Ammonia by Heterogeneous Catalysis in a Packed-Bed Dielectric-Barrier Discharge: Influence of Argon Addition and Voltage. *IEEE Trans. Plasma Sci.* **2014**, *42* (10), 2338−2339.
(19) van Helden, J. H.; Wagemans, W.; Yagci, G.; Zijlmans, R. A. B.; Schram, D. C.; Engeln, R.; Lombardi, G.; Stancu, G. D.; Röpcke, J. Detailed Study of the Plasma-Activated Catalytic Generation of Ammonia in N2-H2 Plasmas. *J. Appl. Phys.* **2007**, *101* (4), 043305.
(20) Hong, J.; Pancheshnyi, S.; Tam, E.; Lowke, J. J.; Prawer, S.; Murphy, A. B. Kinetic Modelling of NH 3 Production in N 2 − H 2 Non-Equilibrium Atmospheric-Pressure Plasma Catalysis. *J. Phys. D Appl. Phys.* **2017**, *50* (15), 154005.
(21) Mehta, P.; Barboun, P.; Herrera, F. A.; Kim, J.; Rumbach, P.; Go, D. B.; Hicks, J. C.; Schneider, W. F. Overcoming Ammonia Synthesis Scaling Relations with Plasma-Enabled Catalysis. *Nat. Catal.* **2018**, *1* (4), 269−275.
(22) Mehta, P.; Barboun, P. M.; Engelmann, Y.; Go, D. B.; Bogaerts, A.; Schneider, W. F.; Hicks, J. C. Plasma-Catalytic Ammonia Synthesis beyond the Equilibrium Limit. *ACS Catal.* **2020**, *10* (12), 6726−6734.
(23) Rouwenhorst, K. H. R.; Kim, H.-H.; Lefferts, L. Vibrationally Excited Activation of N2 in Plasma-Enhanced Catalytic Ammonia Synthesis: A Kinetic Analysis. *ACS Sustain. Chem. Eng.* **2019**, *7* (20), 17515−17522.
(24) Hong, J.; Prawer, S.; Murphy, A. B. Plasma Catalysis as an Alternative Route for Ammonia Production: Status, Mechanisms, and Prospects for Progress. *ACS Sustain. Chem. Eng.* **2018**, *6* (1), 15−31.
(25) Patil, B. S.; Cherkasov, N.; Srinath, N. V.; Lang, J.; Ibhadon, A. O.; Wang, Q.; Hessel, V. The Role of Heterogeneous Catalysts in the Plasma-Catalytic Ammonia Synthesis. *Catal. Today* **2021**, *362*, 2−10.
(26) Barboun, P.; Mehta, P.; Herrera, F. A.; Go, D. B.; Schneider, W. F.; Hicks, J. C. Distinguishing Plasma Contributions to Catalyst Performance in Plasma-Assisted Ammonia Synthesis. *ACS Sustain. Chem. Eng.* **2019**, *7* (9), 8621−8630.
(27) Wang, Y.; Craven, M.; Yu, X.; Ding, J.; Bryant, P.; Huang, J.; Tu, X. Plasma-Enhanced Catalytic Synthesis of Ammonia over a Ni/Al2O3 Catalyst at Near-Room Temperature: Insights into the Importance of the Catalyst Surface on the Reaction Mechanism. *ACS Catal.* **2019**, *9*, 10780−10793.
(28) Neyts, E. C. Plasma-Surface Interactions in Plasma Catalysis. *Plasma Chem. Plasma Process.* **2016**, *36* (1), 185−212.
(29) Tu, X.; Gallon, H. J.; Whitehead, J. C. Electrical and Spectroscopic Diagnostics of a Single-Stage Plasma-Catalysis System: Effect of Packing with TiO2. *J. Phys. D Appl. Phys.* **2011**, *44* (48), 482003.
(30) Chen, Z.; Koel, B. E.; Sundaresan, S. Plasma-Assisted Catalysis for Ammonia Synthesis in a Dielectric Barrier Discharge Reactor: Key Surface Reaction Steps and Potential Causes of Low Energy Yield. *J. Phys. D Appl. Phys.* **2022**, *55* (5), 055202.
(31) Wang, J.; Zhang, K.; Mertens, M.; Bogaerts, A.; Meynen, V. Plasma-Based Dry Reforming of Methane in a Dielectric Barrier Discharge Reactor: Importance of Uniform (Sub)Micron Packings/Catalysts to Enhance the Performance. *Appl. Catal., B* **2023**, *337*, 122977.
(32) Kogelschatz, U. Dielectric-Barrier Discharges: Their History, Discharge Physics, and Industrial Applications. *Plasma Chem. Plasma Process.* **2003**, *23* (1), 1−46.
(33) Neyts, E. C.; Ostrikov, K.; Sunkara, M. K.; Bogaerts, A.; Bogaerts, A. Plasma Catalysis: Synergistic Effects at the Nanoscale. *Chem. Rev.* **2015**, *115* (24), 13408−13446.
(34) Whitehead, J. C. Plasma−Catalysis: The Known Knowns, the Known Unknowns and the Unknown Unknowns. *J. Phys. D Appl. Phys.* **2016**, *49* (24), 243001.
(35) Whitehead, J. C. Plasma-Catalysis: Is It Just a Question of Scale? *Front Chem. Sci. Eng.* **2019**, *13* (2), 264−273.
(36) Tu, X.; Gallon, H. J.; Whitehead, J. C. Transition Behavior of Packed-Bed Dielectric Barrier Discharge in Argon. *IEEE Trans. Plasma Sci.* **2011**, *39* (11), 2172−2173.
(37) Ndayirinde, C.; Gorbanev, Y.; Ciocarlan, R.-G.; De Meyer, R.; Smets, A.; Vlasov, E.; Bals, S.; Cool, P.; Bogaerts, A. Plasma-Catalytic Ammonia Synthesis: Packed Catalysts Act as Plasma Modifiers. *Catal. Today* **2023**, *419*, 114156.
(38) Michielsen, I.; Van Laer, K.; Uytdenhouwen, Y.; Meynen, V.; Bogaerts, A. *Packing Effect of SiO2, ZrO2 and Al2O3 Beads on CO2 Conversion in a Packed-Bed DBD Reactor*. In *In International Symposium on Plasma Chemistry*: Antwerp, 2015.
(39) Inan, U. S.; Gołkowski, M. The Plasma Sheath and the Langmuir Probe. In *Principles of Plasma Physics for Engineers and Scientists*; Cambridge University Press: Cambridge, 2010; pp 251−260..
(40) Zhang, Q.-Z.; Bogaerts, A. Propagation of a Plasma Streamer in Catalyst Pores. *Plasma Sources Sci. Technol.* **2018**, *27* (3), 035009.
(41) Zhang, Y.-R.; Neyts, E. C.; Bogaerts, A. Influence of the Material Dielectric Constant on Plasma Generation inside Catalyst Pores. *J. Phys. Chem. C* **2016**, *120* (45), 25923−25934.
(42) Zhang, Q.-Z.; Wang, W.-Z.; Bogaerts, A. Importance of Surface Charging during Plasma Streamer Propagation in Catalyst Pores. *Plasma Sources Sci. Technol.* **2018**, *27* (6), 065009.
(43) Chen, Z.; Jaiswal, S.; Diallo, A.; Sundaresan, S.; Koel, B. E. Effect of Porous Catalyst Support on Plasma-Assisted Catalysis for Ammonia Synthesis. *J. Phys. Chem. A* **2022**, *126* (46), 8741−8752.
(44) Vakili, R.; Gholami, R.; Stere, C. E.; Chansai, S.; Chen, H.; Holmes, S. M.; Jiao, Y.; Hardacre, C.; Fan, X. Plasma-Assisted Catalytic Dry Reforming of Methane (DRM) over Metal-Organic Frameworks (MOFs)-Based Catalysts. *Appl. Catal., B* **2020**, *260*, 118195.
(45) Holzer, F.; Roland, U.; Kopinke, F.-D. Combination of Non-Thermal Plasma and Heterogeneous Catalysis for Oxidation of Volatile Organic Compounds Part 1. Accessibility of the Intra-Particle Volume. *Appl. Catal., B* **2002**, *38* (3), 163−181.
(46) Wang, J.; Zhang, K.; Bogaerts, A.; Meynen, V. 3D Porous Catalysts for Plasma-Catalytic Dry Reforming of Methane: How Does

the Pore Size Affect the Plasma-Catalytic Performance? *Chem. Eng. J.* **2023**, *464*, 142574.
(47) Gorky, F.; Guthrie, S. R.; Smoljan, C. S.; Crawford, J. M.; Carreon, M. A.; Carreon, M. L. Plasma Ammonia Synthesis over Mesoporous Silica SBA-15. *J. Phys. D Appl. Phys.* **2021**, *54* (26), 264003.
(48) Chen, J.; Tang, T.; Wu, X.; Li, C.; Su, X.; Rac, V.; Rakić, V.; Du, X. Unlocking Efficient Synergistic Plasma-Catalyst Ammonia Synthesis: System Optimization and Catalyst Support Screening. *Energy Fuels* **2024**, *38* (11), 10345−10356.
(49) Rouwenhorst, K. H. R.; Mani, S.; Lefferts, L. Improving the Energy Yield of Plasma-Based Ammonia Synthesis with In Situ Adsorption. *ACS Sustain. Chem. Eng.* **2022**, *10* (6), 1994−2000.
(50) Maciver, D. S.; Tobin, H. H.; Barth, R. T. Catalytic Aluminas I. Surface Chemistry of Eta and Gamma Alumina. *J. Catal.* **1963**, *2*, 485−497.
(51) Gorky, F.; Carreon, M. A.; Carreon, M. L. Experimental Strategies to Increase Ammonia Yield in Plasma Catalysis over LTA and BEA Zeolites. *IOP SciNotes* **2020**, *1* (2), 024801.
(52) Xie, Q.; Zhuge, S.; Song, X.; Lu, M.; Ruan, R.; Nie, Y.; Ji, J. Hydrogenation of Plasma-Excited Nitrogen over an Alumina Catalyst for Ammonia Synthesis. *Int. J. Hydrogen Energy* **2018**, *43* (32), 14885−14891.
(53) Wang, Y.; Yang, W.; Xu, S.; Zhao, S.; Chen, G.; Weidenkaff, A.; Hardacre, C.; Fan, X.; Huang, J.; Tu, X. Shielding Protection by Mesoporous Catalysts for Improving Plasma-Catalytic Ambient Ammonia Synthesis. *J. Am. Chem. Soc.* **2022**, *144* (27), 12020−12031.
(54) Wei, J.; Ren, Y.; Luo, W.; Sun, Z.; Cheng, X.; Li, Y.; Deng, Y.; Elzatahry, A. A.; Al-Dahyan, D.; Zhao, D. Ordered Mesoporous Alumina with Ultra-Large Pores as an Efficient Absorbent for Selective Bioenrichment. *Chem. Mater.* **2017**, *29* (5), 2211−2217.
(55) Li, H.; Zhang, L.; Dai, H.; He, H. Facile Synthesis and Unique Physicochemical Properties of Three-Dimensionally Ordered Macroporous Magnesium Oxide, Gamma-Alumina, and Ceria−Zirconia Solid Solutions with Crystalline Mesoporous Walls. *Inorg. Chem.* **2009**, *48* (10), 4421−4434.
(56) Yuan, Q.; Yin, A.-X.; Luo, C.; Sun, L.-D.; Zhang, Y.-W.; Duan, W.-T.; Liu, H.-C.; Yan, C.-H. Facile Synthesis for Ordered Mesoporous γ-Aluminas with High Thermal Stability. *J. Am. Chem. Soc.* **2008**, *130* (11), 3465−3472.
(57) Wu, Q.; Zhang, F.; Yang, J.; Li, Q.; Tu, B.; Zhao, D. Synthesis of Ordered Mesoporous Alumina with Large Pore Sizes and Hierarchical Structure. *Microporous Mesoporous Mater.* **2011**, *143* (2−3), 406−412.
(58) Xu, X.; Megarajan, S. K.; Zhang, Y.; Jiang, H. Ordered Mesoporous Alumina and Their Composites Based on Evaporation Induced Self-Assembly for Adsorption and Catalysis. *Chem. Mater.* **2020**, *32* (1), 3−26.
(59) Babaei, Z.; Najafi Chermahini, A.; Dinari, M. Alumina-Coated Mesoporous Silica SBA-15 as a Solid Catalyst for Catalytic Conversion of Fructose into Liquid Biofuel Candidate Ethyl Levulinate. *Chem. Eng. J.* **2018**, *352*, 45−52.
(60) Zhao, D.; Huo, Q.; Feng, J.; Chmelka, B. F.; Stucky, G. D. Nonionic Triblock and Star Diblock Copolymer and Oligomeric Surfactant Syntheses of Highly Ordered, Hydrothermally Stable, Mesoporous Silica Structures. *J. Am. Chem. Soc.* **1998**, *120*, 6024−6036.
(61) Sun, Y.-H.; Sun, L.-B.; Li, T.-T.; Liu, X.-Q. Modulating the Host Nature by Coating Alumina: A Strategy to Promote Potassium Nitrate Decomposition and Superbasicity Generation on Mesoporous Silica SBA-15. *J. Phys. Chem. C* **2010**, *114* (44), 18988−18995.
(62) Kruk, M.; Cao, L. Pore Size Tailoring in Large-Pore SBA-15 Silica Synthesized in the Presence of Hexane. *Langmuir* **2007**, *23* (13), 7247−7254.
(63) Kruk, M.; Jaroniec, M.; Ko, C. H.; Ryoo, R. Characterization of the Porous Structure of SBA-15. *Chem. Mater.* **2000**, *12* (7), 1961−1968.
(64) Feng, P.; Bu, X.; Pine, D. J. Control of Pore Sizes in Mesoporous Silica Templated by Liquid Crystals in Block Copolymer−Cosurfactant−Water Systems. *Langmuir* **2000**, *16* (12), 5304−5310.
(65) Butterworth, T.; Elder, R.; Allen, R. Effects of Particle Size on CO2 Reduction and Discharge Characteristics in a Packed Bed Plasma Reactor. *Chem. Eng. J.* **2016**, *293*, 55−67.
(66) Launer, P.; Arkles, B. Infrared Analysis of Organosilicon Compounds: Spectra-Structure Correlations. In *Silicon Compounds: Silanes & Silicones*; Arkles, B., Larson, G., Eds.; Gelest Inc., 2013; pp 175−178. Morrisville.
(67) Thommes, M.; Kaneko, K.; Neimark, A. V.; Olivier, J. P.; Rodriguez-Reinoso, F.; Rouquerol, J.; Sing, K. S. W. Physisorption of Gases, with Special Reference to the Evaluation of Surface Area and Pore Size Distribution (IUPAC Technical Report). *Pure Appl. Chem.* **2015**, *87* (9−10), 1051−1069.
(68) Sing, K. S. W.; Everett, D. H.; Haul, R. A. W.; Moscou, L.; Pierotti, R. A.; Rouquerol, J.; Siemieniewska, T. Reporting Physisorption Data for Gas/Solid Systems with Special Reference to the Determination of Surface Area and Porosity; **1985**, *57*, 4, 603-619.
(69) Impéror-Clerc, M.; Davidson, P.; Davidson, A. Existence of a Microporous Corona around the Mesopores of Silica-Based SBA-15 Materials Templated by Triblock Copolymers. *J. Am. Chem. Soc.* **2000**, *122* (48), 11925−11933.
(70) Kruk, M.; Jaroniec, M.; Ko, C. H.; Ryoo, R. Characterization of the Porous Structure of SBA-15. *Chem. Mater.* **2000**, *12* (7), 1961−1968.
(71) Coasne, B.; Galarneau, A.; Di Renzo, F.; Pellenq, R. J. M. Gas Adsorption in Mesoporous Micelle-Templated Silicas: MCM-41, MCM-48, and SBA-15. *Langmuir* **2006**, *22* (26), 11097−11105.
(72) Wang, Y.; Yang, W.; Xu, S.; Zhao, S.; Chen, G.; Weidenkaff, A.; Hardacre, C.; Fan, X.; Huang, J.; Tu, X. Shielding Protection by Mesoporous Catalysts for Improving Plasma-Catalytic Ambient Ammonia Synthesis. *J. Am. Chem. Soc.* **2022**, *144* (27), 12020−12031.

https://doi.org/10.1021/acs.energyfuels.4c03270
Energy Fuels 2024, 38, 23150−23166